UCRL 8966

UNIVERSITY OF CALIFORNIA

Ernest O. Lawrence Radiation Laboratory

5-BEV NEUTRON CROSS SECTIONS IN HYDROGEN AND OTHER ELEMENTS

TWO-WEEK LOAN COPY

This is a Library Circulating Copy which may be borrowed for two weeks. For a personal retention copy, call Tech. Info. Division, Ext. 5545

DISCLAIMER

This document was prepared as an account of work sponsored by the United States Government. While this document is believed to contain correct information, neither the United States Government nor any agency thereof, nor the Regents of the University of California, nor any of their employees, makes any warranty, express or implied, or assumes any legal responsibility for the accuracy, completeness, or usefulness of any information, apparatus, product, or process disclosed, or represents that its use would not infringe privately owned rights. Reference herein to any specific commercial product, process, or service by its trade name, trademark, manufacturer, or otherwise, does not necessarily constitute or imply its endorsement, recommendation, or favoring by the United States Government or any agency thereof, or the Regents of the University of California. The views and opinions of authors expressed herein do not necessarily state or reflect those of the United States Government or any agency thereof or the Regents of the University of California.

UCRL-8966
Physics and Mathematics
TID-4500 (15th Ed.)

pages 17+18 corrected

UNIVERSITY OF CALIFORNIA
Lawrence Radiation Laboratory
Berkeley, California

Contract No. W-7405-eng-48

5-BEV NEUTRON CROSS SECTIONS IN HYDROGEN AND OTHER ELEMENTS

John H. Atkinson

(Thesis)

November 4, 1959

Printed for the U.S. Atomic Energy Commission

Printed in USA. Price $2.25. Available from the
Office of Technical Services
U. S. Department of Commerce
Washington 25, D.C.

5-BEV NEUTRON CROSS SECTIONS IN HYDROGEN AND OTHER ELEMENTS

Contents

Abstract 4

I. Introduction 5

II. Experimental Method

A. Experimental Arrangement

1. Beam 6
2. Monitor 8
3. Detector 10
4. Electronics 13

B. Gas Čerenkov Counters

1. Theory 16
2. Description of Counter 17
3. Performance 19
4. Discussion 19

C. Neutron Energy

1. Distribution 22
2. Assumptions 27

D. Counting Rates

1. Neutron Production in the Bevatron Target . 30
2. Attenuation and Solid Angle 31
3. Detector Efficiency 32
4. Total Counting Rate 33
5. Monitor Counting Rate 34

III. Results

A. Cross-Section Measurements

1. Transmission Measurement 35
2. Geometric Corrections 37
3. Results 42

B. Errors
1. Beam Contamination 49
2. Geometry 50
3. Bevatron Proton Beam Tracking 52
4. Counting Statistics and Total Error . . . 53
IV. Conclusions
A. Discussion
1. Comparison with Previous Experiments . . 55
2. Nucleon-Nucleon Cross Sections 55
B. Interpretation
1. Generalized Diffraction Theory 60
2. Application of Theory to Experiments . . 67
C. Optical Model
1. Theory 68
2. Optical-Model Parameters 70
3. Optical-Model Results 76
Acknowledgments 77

5-BEV NEUTRON CROSS SECTIONS IN HYDROGEN AND OTHER ELEMENTS

John H. Atkinson

Lawrence Radiation Laboratory
University of California
Berkeley, California

November 4, 1959

ABSTRACT

This experiment measures the neutron total and reaction cross sections at 5.0 Bev. Transmission measurements were made in good and poor gemetry. A high-energy neutron beam is produced when the Bevatron circulating proton beam strikes a copper target. Neutrons are identified by their production of pions in a beryllium block, which are then detected by a counter telescope including a gas Čerenkov counter. The threshold of this gas Čerenkov counter limits the mean effective neutron energy to 5.0 ± 0.4 Bev.

The cross sections measured for the various elements are (in millibarns):

	Pb	Sn	Cu	Al	C	H
σ_t	2534 ± 105	1986 ± 88	1158 ± 34	614 ± 33	319 ± 20	33.6 ± 1.6
σ_r	1670 ± 79		586 ± 25	381 ± 27	235 ± 16	

The 5-Bev total cross sections are 20% below the total cross sections measured at 1.4 Bev by Coor et al.,[1] whereas the reaction cross sections remain essentially constant as a function of energy. This behavior of the cross sections is interpreted by a generalized diffraction theory developed by Glassgold and Greider.

I. INTRODUCTION

This experiment extends the knowledge of the neutron total and reaction cross sections from 1.4 Bev to 5.0 Bev. The Brookhaven data of Coor et al. at 1.4 Bev indicated that the neutron total cross sections were rising sharply with energy at 1.4 Bev.[1] Robert Williams[2] made the prediction based on these data and some high-energy cosmic-ray data, that the nucleon-nucleon total cross section would be found to rise monotonically from 42 millibarns at 1.4 Bev to 120 mb at 30 Bev. This prediction became open to question with the publication of the high-energy p-p elastic scattering data of Cork, Wenzel, and Causey,[3] which showed a decrease in the elastic-scattering cross section from a peak at 1.5 Bev.

The total and reaction cross sections were measured for 5-Bev neutrons in lead, copper, aluminum, and carbon to an accuracy of about 5%. The total n-p cross section was measured directly by the use of a 7-foot-long liquid hydrogen target. A gas Čerenkov counter was used in this experiment to place limits on the effective neutron energy. The threshold of the Čerenkov counter for pions produced by the neutron beam establishes a minimum neutron energy of 3.5 Bev, while the maximum energy available is the 6.2-Bev peak energy of the Bevatron. Knowledge of the neutron energy is critical for the determination of meaningful cross sections, and is quite difficult to achieve with high-energy neutron beams.

The experiment is interpreted by a new theory developed by Glassgold and Greider[4] to interpret high-energy scattering data. This generalized diffraction theory gives expressions for the total and reaction cross sections in easily calculable closed forms that fit the neutron scattering data well from 300 Mev to 5 Bev. A simple optical model is also fitted to our data, which gives a check on our energy determination as well as the usual optical-model parameters.

II. EXPERIMENTAL METHOD

A. Experimental Arrangement

1. Beam

The neutron beam is generated by the Bevatron internal proton beam striking the 72° 31' Q III target. This is a $1/2 \times 1/2 \times 3$-inch copper flip-up target with the 3-inch dimension tangent to the circulating proton beam. This target was designed to produce a low-energy K^- beam for the Alvarez 10-and 15-inch hydrogen bubble chambers. It operated a large part of the time and was effective in producing neutrons. Whenever the primary proton beam is spilled on a target, charge-exchange neutrons are produced in the forward direction. The neutron yield is possibly increased by multiple traversals of this relatively short target by the circulating proton beam.

Protons scattered from targets at larger radii spiral in and produce a usable neutron beam in our target. Since our target is at a mean radius of 597-5/16 in., most other Bevatron targets were substantially outside this radius, making it possible to run on a noninterfering basis. More than half the data of this experiment were taken with beam scavenged in this manner. The internal target must be raised to give an appreciable neutron beam. There is a factor-of-100 difference in the neutron counting rates with the 597-5/16-in. target in and out.

The neutron beam for this experiment was taken at 0° from the target, since there is maximum neutron flux in the forward direction. The neutrons emerged from the north straight section of the Bevatron with a 4-in. path length in the steel structure of the straight section. The beam path is illustrated in Fig. 1. The neutron beam is collimated as it passes through the Bevatron shielding wall by a $2 \times 2 \times 60$-in. aperture in 5 ft of lead. The entrance to the collimator is 45 ft from the Bevatron target, subtending the small half angle of 0.114-deg. Two 1-in. lead bricks, placed 6 in. apart in the mouth of the collimator, are an effective γ-ray filter, since the stray field of the Bevatron sweeps away all electrons produced.

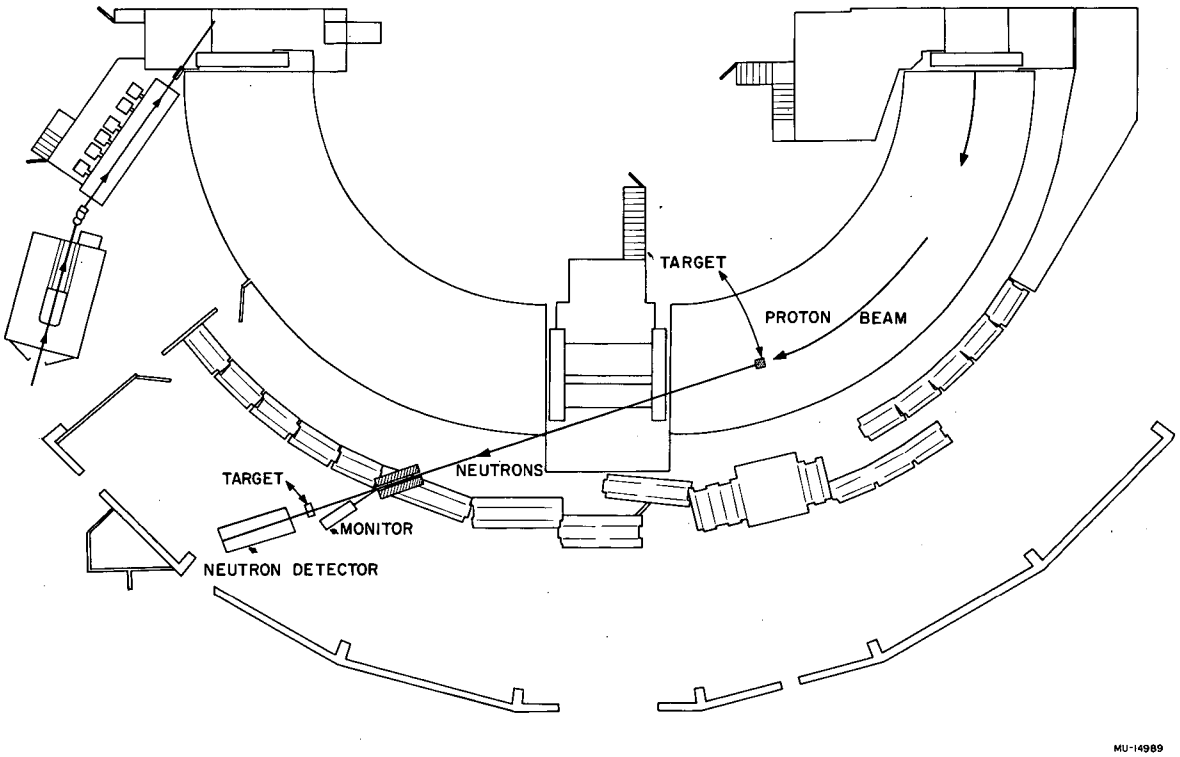

Fig. 1. Path of the neutron beam from the Bevatron through the detector. This shows the original monitor.

2. Monitor

As the Bevatron proton-beam flux is highly variable from pulse to pulse, this experiment required an accurate monitor which would count at a rate proportional to the high-energy neutron flux in the channel. The first monitor used was a triple-coincidence 4-in. scintillation counter telescope. This telescope looked at a 20-deg angle at a 1-in.-thick block of polyethylene located in the downstream exit of the collimator. Charged particles produced by the neutron flux passing through the polyethylene were counted by the telescope in numbers proportional to the neutron flux. The 20-deg angle of the telescope and 2 in. of lead placed between the second and third counters selected high-energy charged particles. This monitor was satisfactory only for stable operating conditions of the Bevatron.

However, most of the charged particles counted by the telescope were produced in or scattered from the sides of the collimator. Also, the proportionality between monitor counts and neutron counts was dependent on the operating conditions and tracking of the Bevatron, since the monitor telescope had much cruder energy discrimination than the neutron detector. The ratio of charged to neutral particles in our beam was also dependent on Bevatron beam tracking. Since this is a relative transmission measurement, adjacent runs (with similar beam conditions) gave valid cross sections; even so, the monitor-induced variations in relative counting rates prohibited the effective combination of enough data to give efficient statistical use of beam time.

Our second and more satisfactory monitor uses a gas Čerenkov counter and two 4×4-in. plastic scintillators, in triple coincidence, placed immediately after the collimator in series with the neutron beam. This monitor is illustrated in Fig. 2. The Čerenkov counter contains 15 psig of Freon-12 (CCl_2F_2), and counts charged pions, of energy greater than 2.4 Bev, produced in the γ-ray filter at the entrance of the collimator and in the walls of the collimator. The two plastic scintillators determine the geometry of the monitor telescope,

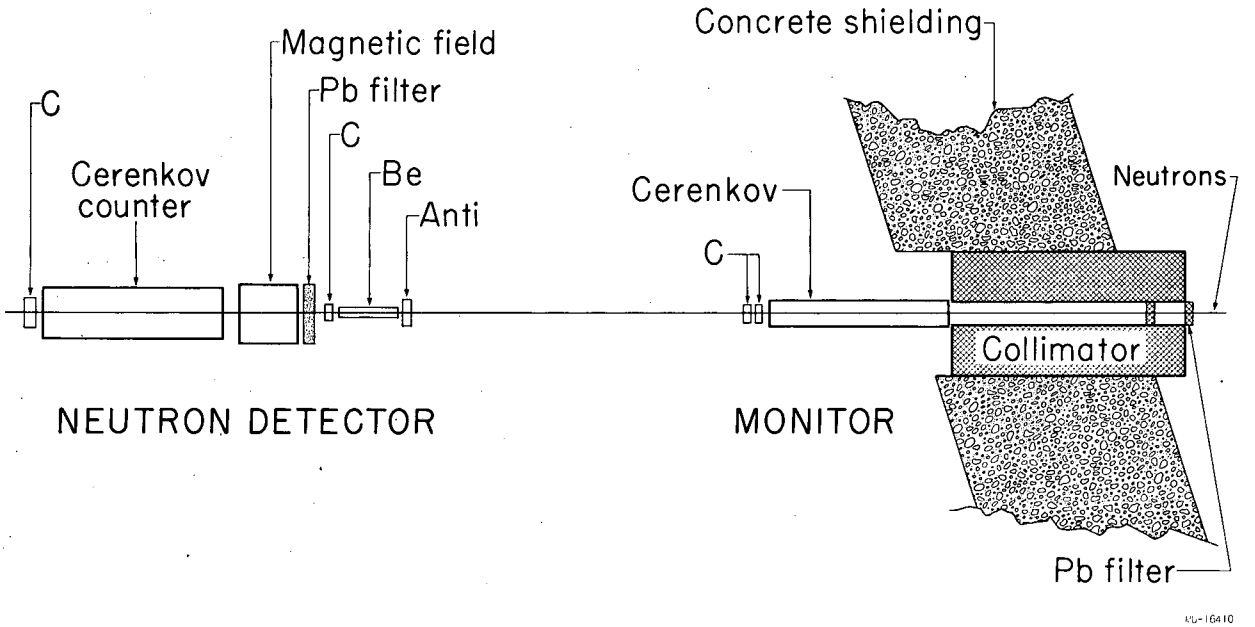

Fig. 2. Experimental arrangement (schematic representation), showing the collimator, monitor telescope, and neutron-detector telescope.

and eliminate accidental counts through the requirement for a triple coincidence. The last element of the monitor is 18 ft from the γ-ray filter, subtending a half angle of 0.53 deg, and is 63 ft from the Bevatron target, subtending an angle of 0.152 deg. There is 24 ft between the monitor and the neutron detector, allowing both good-and poor-geometry absorber positions. For most of the data taken in this experiment this monitor was used.

3. Detector

The neutron detector is illustrated in Fig. 2. The first element of the neutron detector is a 6X6X1-in. plastic scintillation counter connected in anticoincidence to the neutron coincidence circuit ("anti-counter"). This counter eliminates detector counts from charged particles in the beam. Since it is well plateaued, it is close to 100% efficient. The large size of this counter in comparison with the 2X2-in. beam cross section reduces the background caused by charged particles scattering into later elements of the detector.

Following the anticounter, the neutrons are converted into charged pions for counting purposes in a 12X2X2-in. beryllium block. For some poor-geometry measurements, an aluminum block was used as a converter because of its shorter length (8X2X2 in.). The beryllium is a more efficient neutron converter than aluminum, since a large cross section for inelastic neutron events and a low total cross section for the pions produced gives an effective converter. The maximum conversion efficiency is 0.384 for 12 in. of beryllium and 0.250 for 8 in. of aluminum. These calculated efficiencies assume that all inelastic neutron events in the converter produce high-energy pions in the forward direction. The pions produced are considered lost if they interact or scatter in leaving the converter.

Following the converter is a 2X2X1-in. plastic scintillator, which counts charged particles produced in the converter and is connected in coincidence with the two following counters in the detector. This counter in conjunction with the converter forms the geometry-determining element of the measurement.

Charged pions of sufficient energy are then detected by a 10-in.-diameter gas Čerenkov counter developed for this experiment. The gas Čerenkov counters are energy-threshold detectors and determine the effective neutron energy. (These counters, crucial to this experiment, are described in detail in Section II. B.) The detector Čerenkov counter is filled with Freon-12 (CCl_2F_2) at 30 psig. This gives an absolute threshold of 1.56 Bev for charged pions. However, the threshold efficiency of the counter is not a step function, and the minimum effective pion energy is 1.85 Bev for 50% counting efficiency. From the minimum pion energy a minimum energy for the converted neutrons is derived. The effective energy distribution of the neutrons is discussed in Section II.C.

Another element is necessary in the detector. Neutral pions are produced in the converter with a multiplicity of about 1/3. The neutral pions decay to two gamma rays essentially where they are produced. Some of these gamma rays produce electron pairs in the converter. These electrons are counted by the following scintillation counters and the gas Čerenkov counter. This destroys energy discrimination of the detector, since even a 15-Mev electron counts. This π^0 contamination was established by inserting various thicknesses of lead after the converter and materializing the gamma rays more efficiently. The initial increase of the counting rate as lead is added is illustrated in Fig. 3. The decrease in the counting rate as excess lead is added is caused by the absorption of pions, photons, and electrons in the lead.

To preserve the energy discrimination of the detector an electron filter was placed immediately before the Čerenkov counter. This filter consists of 2 in. of lead (10 radiation lengths) and a 6-kilogauss magnetic field, plus an inch of iron which also serves as a magnetic shield for the counter following the converter. From approximate shower theory the average energy of the electrons emerging from the lead is given by $E = E_0 \times 2^{-10}$. For a 2-Bev neutral pion this gives an approximate electron energy of 1 Mev. The 6-kilogauss field applied

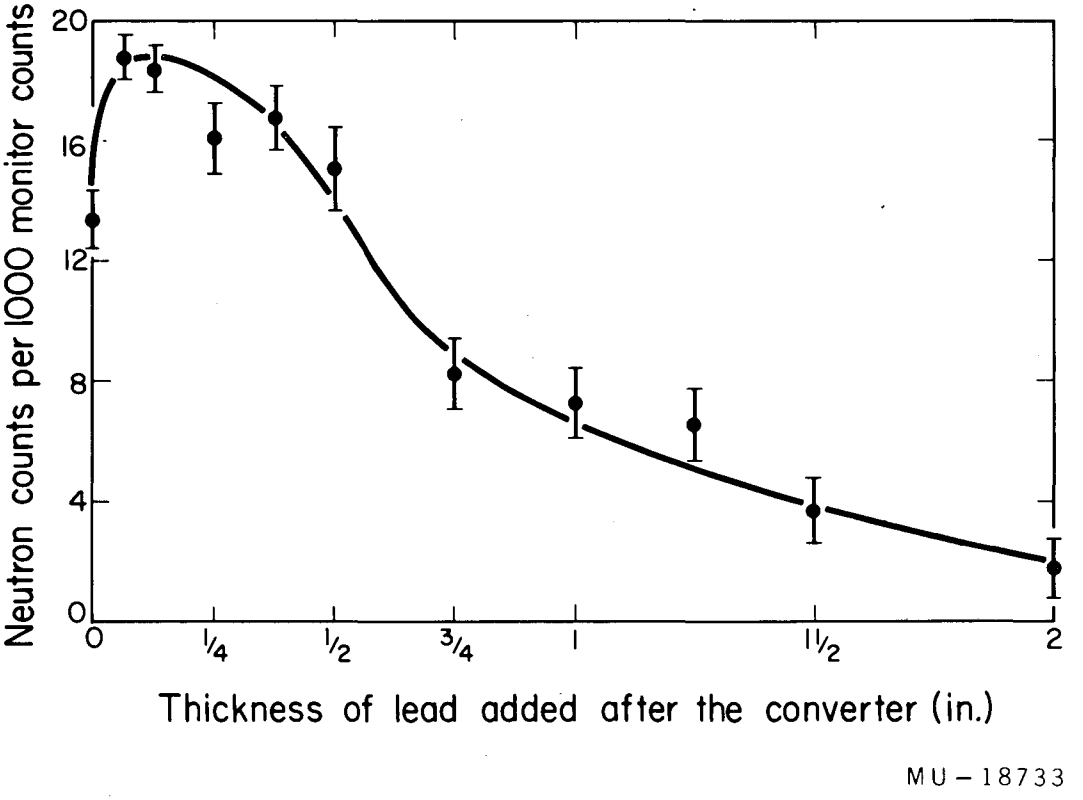

Fig. 3. A counting rate as a function of lead added to the converter. Gamma-ray pairs from π^0 decay produce electron pairs in the converter and the added lead.

over 10 in. sweeps all electrons of energy less than 87 Mev out of the Čerenkov counter but deflects the charged pions less than 1 deg. Experimental calibration of neutron counting rate versus lead thickness and magnet current are illustrated in Fig. 4. These calibrations indicate that the electron filter was just adequate even without the magnetic field.

The counting cycle consisted of a run with a particular absorber thickness in and the converter in, followed by a run with the converter out. The counting rate with the converter out was subtracted as background. Since the counting rates with the converter out were about 1/4 the counting rates with the converter in, the converter-out runs were 1/2 the duration of the converter-in runs to give maximum statistical efficiency. The cycle was then repeated with another absorber thickness. This procedure corrected the experiment for the possible inefficiency of the anticounter and for charged particles scattered into the detector.

4. Electronics

The electronic counting equipment used was generally conventional for the Lawrence Radiation Laboratory. Thus the basic counting setup used for both the monitor and the neutron detector is as illustrated in Fig. 5. The neutron detector adds an "anti" input to eliminate charged particles. Hewlett-Packard prescalers were used in the monitor to permit counting without jamming on the rapid beam-ejector pulse of 10 μsec.

Special attention was given discrimination levels. This experiment required stable discrimination levels, since the effective energy threshold of the Čerenkov counters depends on the size of signal required to register as a count. A Perez-Mendez–Swift discriminator amplifier[5] was used to establish the discrimination levels. The discriminator levels were set so that the scalers would just count with a 2.8-volt signal from a millimicrosecond pulser put into the coincidence circuits. The 2.8-volt level chosen was the midpoint between the tripping level and saturation for the Evans

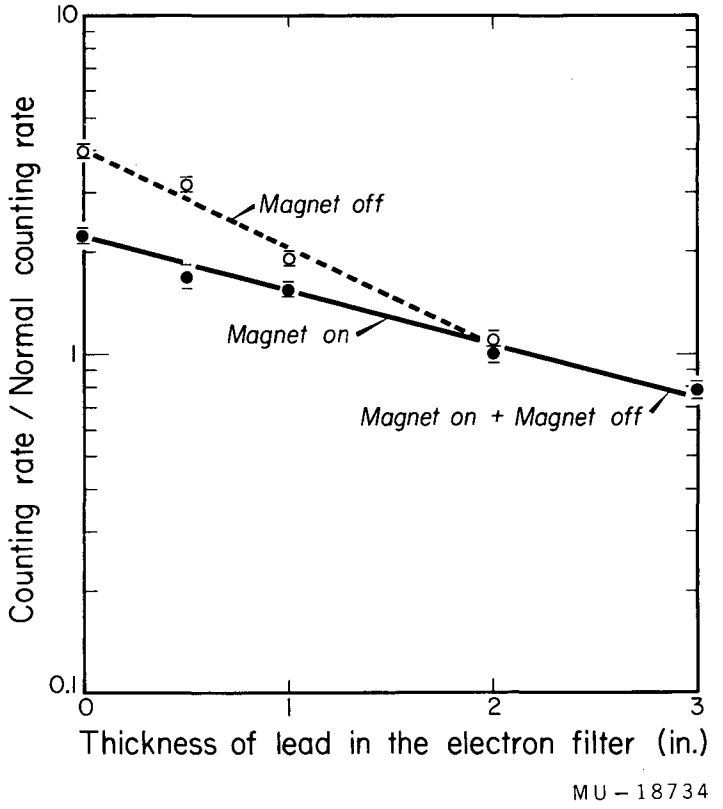

Fig. 4. Effect of the electron filter as a function of the thickness of lead in the filter. The normal operating condition (2 in. of Pb, magnet on) is taken as 1.0 on the ordinate.

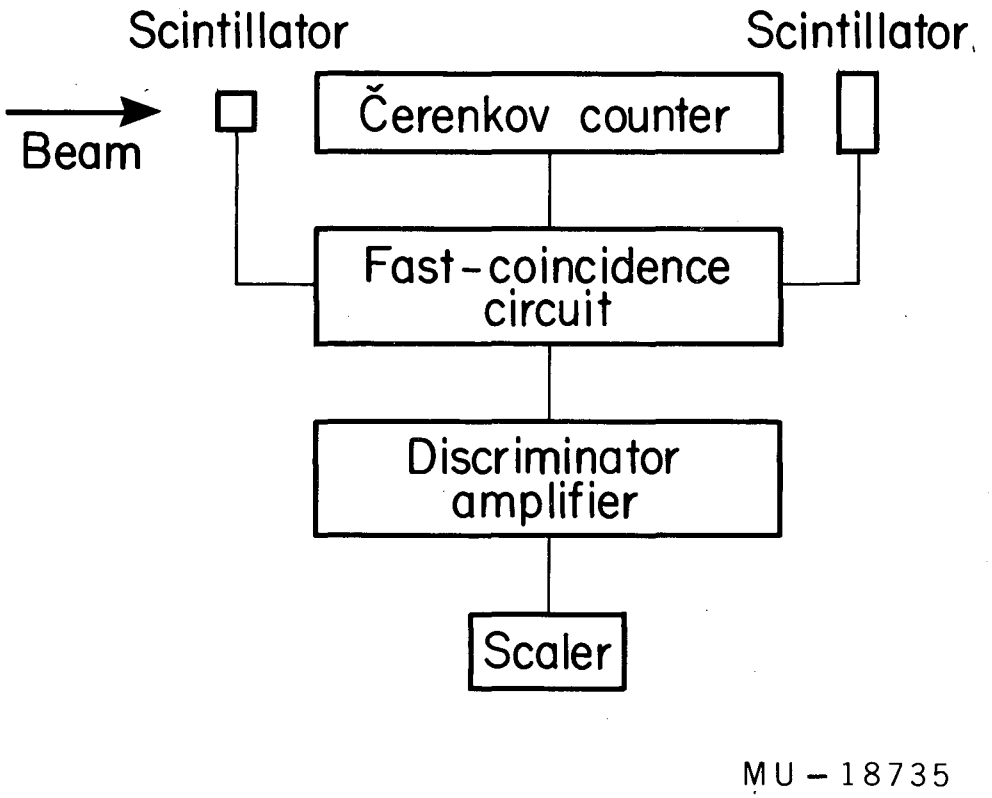

Fig. 5. Block diagram of the basic electronic components.

coincidence circuits used. The actual counter signals exceeded 5 volts in normal operation. The discriminator amplifiers were very stable in operation, requiring a correction not exceeding 0.05 volt in an average week of operation. This high discrimination stability made a great improvement in the tracking and reproducibility of the relative counting rates over the scaler discriminators used earlier.

B. Gas Čerenkov Counters

1. Theory

Čerenkov counters select charged particles on the basis of their relativisitic velocity, β. From the theory of Frank and Tamm,[6] the Čerenkov radiation is confined to a narrow conical shell about the direction of the incoming particle, with the opening angle θ of the cone given by $\cos\theta = 1/n\beta$. Also, the number of light quanta with frequencies between ν and $(\nu + d\nu)$ per unit length of path of the particle with charge e is given by

$$N(\nu)\, d\nu = 4\pi^2 \frac{e^2}{hc^2} \left(1 - \frac{1}{n^2\beta^2}\right) d\nu, \qquad (1)$$

where n is the index of refraction. For a singly charged particle integrated from 3500 to 5600 A (the spectral response of the S-11 photocathode) we have

$$N = 490 \left(1 - \frac{1}{n^2\beta^2}\right), \qquad (2)$$

where N is the number of quanta per centimeter of path length. The velocity selection may be accomplished either by detecting the Čerenkov light within a given angular range, or by using the threshold properties of the Čerenkov effect, i.e., $\beta = \frac{1}{n}$.

In practice the correlation between β and the angle of the Čerenkov light can be used in a velocity-selecting device for particles with values of β less than 0.99 for which the differential change in β corresponds to a physically usable angular interval.[7] However, for higher-energy particles with values of β greater than 0.990, the

LAWRENCE RADIATION LABORATORY
UNIVERSITY OF CALIFORNIA
BERKELEY, CALIFORNIA

ERRATUM

January 20, 1960

FROM: Technical Information Division

TO: Distribution - UCRL-8966

Would you please replace page 17-18 of UCRL-8966, "5-BEV NEUTRON CROSS SECTIONS IN HYDROGEN AND OTHER ELEMENTS", by John H. Atkinson with the attached sheet.

change in angle versus β is too small to be readily useful, and hence it is more practical to use the threshold properties of the Čerenkov effect in this energy region.

The Čerenkov counters used in this experiment are suitable for the detection of particles with values of β ranging from 0.980 to 0.999. The corresponding values of index of refraction for the threshold of the Čerenkov effect range from 1.0204 to 1.00100, which necessitates the use of a radiator in the gaseous phase.

2. Description of Counter

The assembly for the counter used in the monitor is shown in Fig. 6. The gas radiator is contained in the cylindrical steel shell, 6 ft. long and 4 in. in diameter. (Standard 4-in. pipe flanges are used throughout to simplify the construction.) The inner surface of the cylinder is made reflecting by a thin shell of polished aluminum rolled into it. The Čerenkov light is deflected from the beam at the rear of the radiating cylinder by a 45-deg plane front-aluminized mirror. This mirror reflects the light up 90 deg through a Lucite window onto a photomultiplier tube. The window (3/4 in. thick) makes a pressure seal to the gas container and can be used up to pressures of 150 lb/in.^{2}. The small aluminum cone in front of the Lucite window has a polished inner surface and serves to collect some of the light produced by particles that traverse the radiator cylinder slightly off axis. Since the opening angle of the Čerenkov cone is approximately 1 deg, the light is produced in an almost parallel beam.

The photomultiplier tube is a 16-stage RCA C7232A tube; its cathode window is in optical contact with the Lucite window via a thin layer of silicone grease. Adequate magnetic shielding for operation around the Bevatron is provided by a 1/16-in. mu-metal shield and the 1/4-in. iron walls of the multiplier housing.

In order to decrease the number of noise pulses, the photomultiplier is maintained at dry-ice temperature by enclosing its housing in a Styrofoam box filled with dry ice. The photomultiplier housing must then be airtight to prevent moisture from condensing inside the

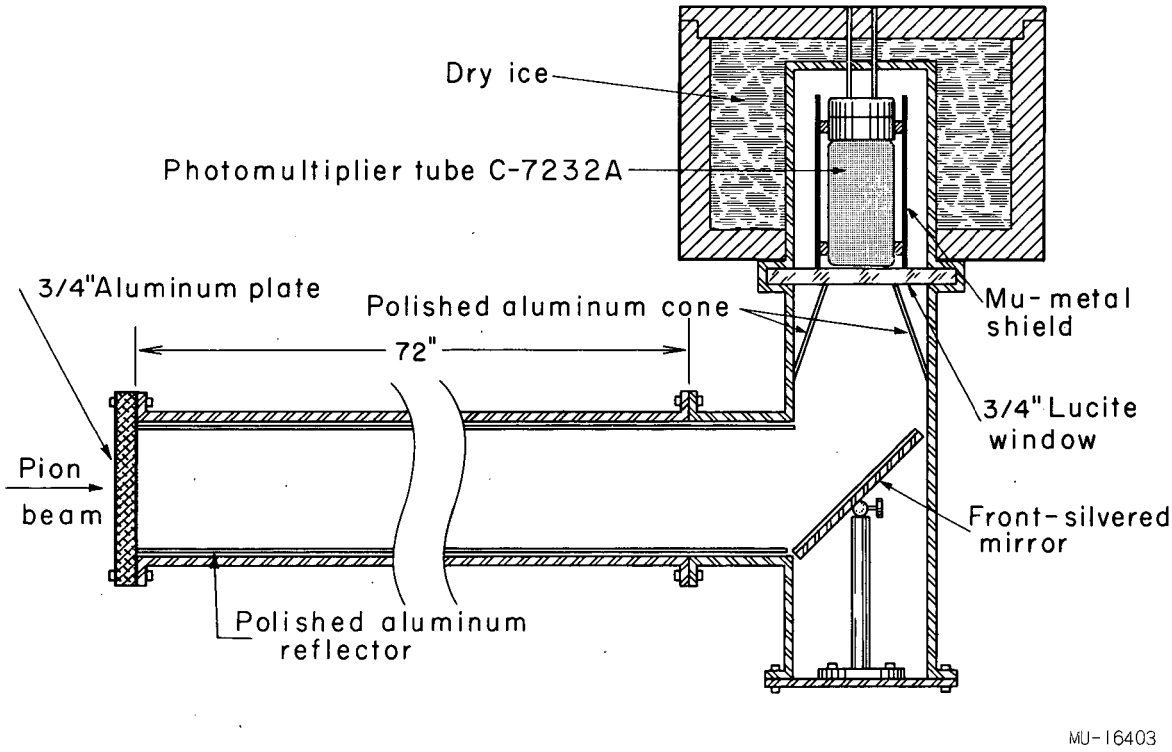

Fig. 6. Cross-sectional view of the 4-in. gas Čerenkov counter used in the monitor counter telescope.

socket assembly. Also, the gas in the counter must be very dry to prevent formation of frost, (which obscures the optical path) on the Lucite window. Silica gel bags packed in the counter under the turning mirror and silica gel refrigeration dryers in the filling lines accomplish this satisfactorily.

3. Performance

The detection efficiency of this counter for counting particles was investigated experimentally by using a monochromatic beam of pions from the Bevatron with a momentum of 3.0 ± 0.1 Bev/c ($\beta = 0.9989$). This calibration experiment is described elsewhere.[8] The efficiency of the Čerenkov counter is defined as the ratio of the number of counts in the Čerenkov counter plus a monitor in coincidence to the number of monitor counts. A plot of the detection efficiency of the Čerenkov counter for 3-Bev pions versus the pressure of gas in the counter is given in Fig. 7. Figure 8 gives the corrected curve with the electron background and the momentum spread of the calibrating pion beam unfolded from the curve.

4. Discussion

A gas Čerenkov counter of the type just described was used originally in the neutron detector, and is used currently in the monitor. A 10-in. diameter gas Čerenkov counter of similar design has been substituted in the neutron detector to collect a larger solid angle of pions produced in the detector. The shape of the threshold efficiency curve was measured, since the energy selection of the counter depends on its effective threshold. From Fig. 8 and Eq. (2), one can calculate the number of photons produced for 90% counting efficiency (213) and 10% efficiency (71) at 1950 volts. Since the phototube is sensitive only in a limited spectral range, these photon numbers are a constant of the counter. For convenience in making the energy-spectrum calculation, the threshold was taken as a step function at the 50% efficiency point (160 photons).

Since the slope of the threshold efficiency of the counter determines

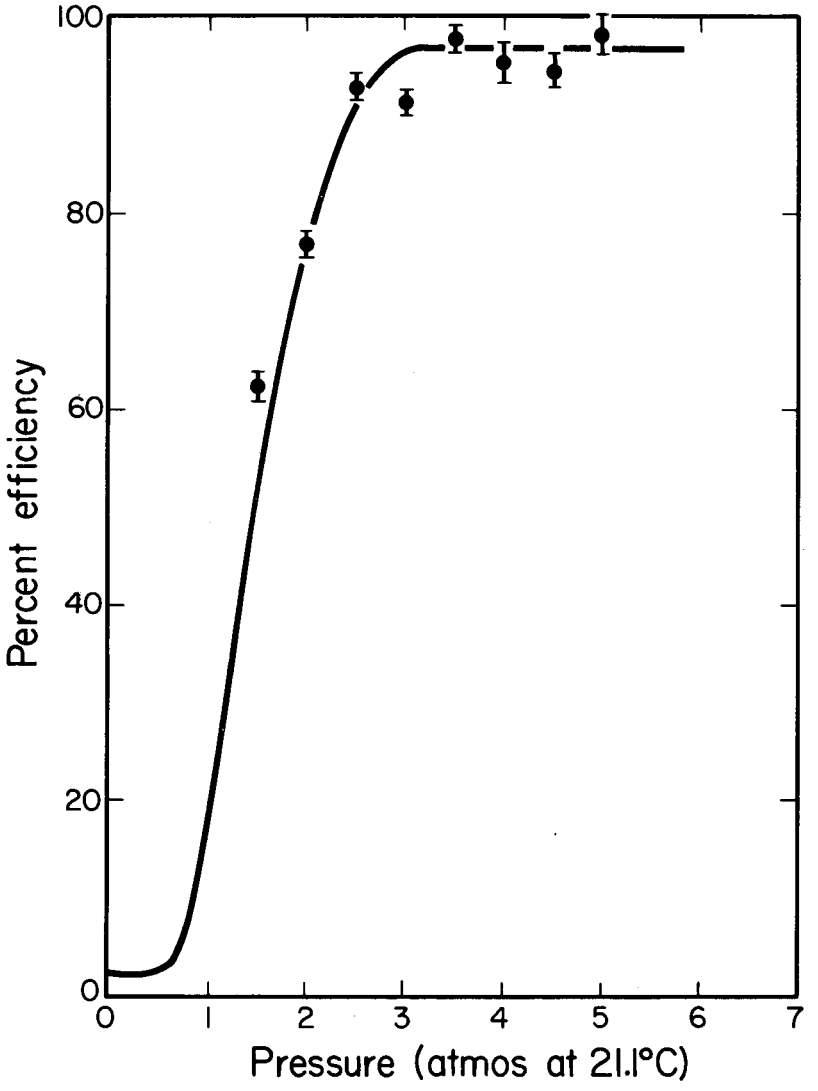

MU-18736

Fig. 7. Measured detection efficiency of CCl_2F_2 Čerenkov counter vs gas pressure for 3-Bev pions. The curve was taken with 1950 volts on the photomultiplier tube.

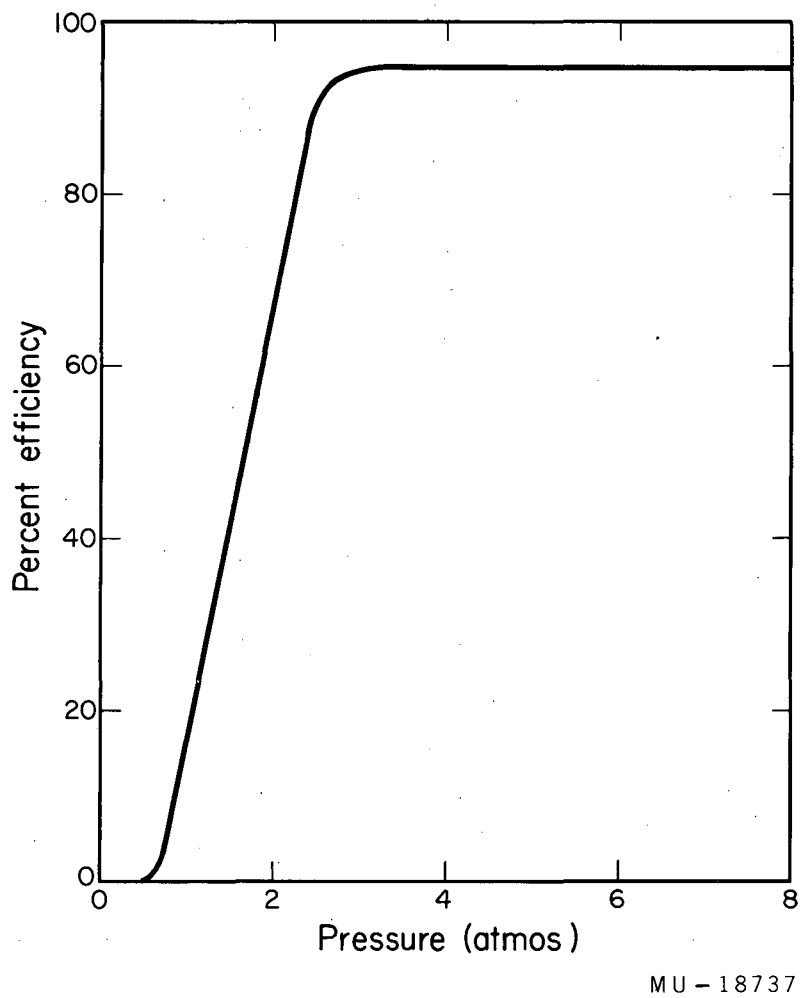

Fig. 8. Corrected curves of efficiency vs pressure. The electron background has been subtracted, and the threshold slope has been corrected for the energy spread of the pion beam.

the discrimination properties of the counter, a detailed study of the causes of this slope was made. The variation of index of refraction of the gas with wave length over the spectral sensitivity of the phototube accounts for less than 30% of the observed slope. The remainder of the slope is essentially due to statistical fluctuations in the small number of photons produced, collected, and converted to photoelectrons in the counter. A statistical analysis indicates that the most important of these causes are (with percentage fluctuation from each process at 90% efficiency given in parenthesis):

a. The small number of photons produced–less than 300 (6%).
b. The variable number of reflections made by photons, depending on their point of origin, and the statistical nature of the microscopic reflection process for individual photons (8.5%).
c. The statistical nature of the limited (20%) photocathode conversion efficiency (8.5%).

The total percentage fluctuation for all calculated processes is 25% at 90% efficiency and 55% at 10% efficiency. Consideration of the effect of a fixed voltage-discrimination level (illustrated in Fig. 9) indicates that the slope is directly proportional to the gain of the phototube, since the statistical fluctuations in output pulse height about the mean correspond to smaller changes in $n\beta$ for higher gain.

C. Neutron Energy

1. Distribution

The effective neutron energy is determined by the energy selectivity of the neutron detector and by the incoming neutron energy spectrum. In this section we obtain and describe the effective neutron energy.

The effective neutron energy distribution is illustrated in Fig. 10. Analysis of this skewed distribution gives the peak at 5.25 Bev with the half-intensity points at +0.65 Bev and -1.0 Bev. From integration

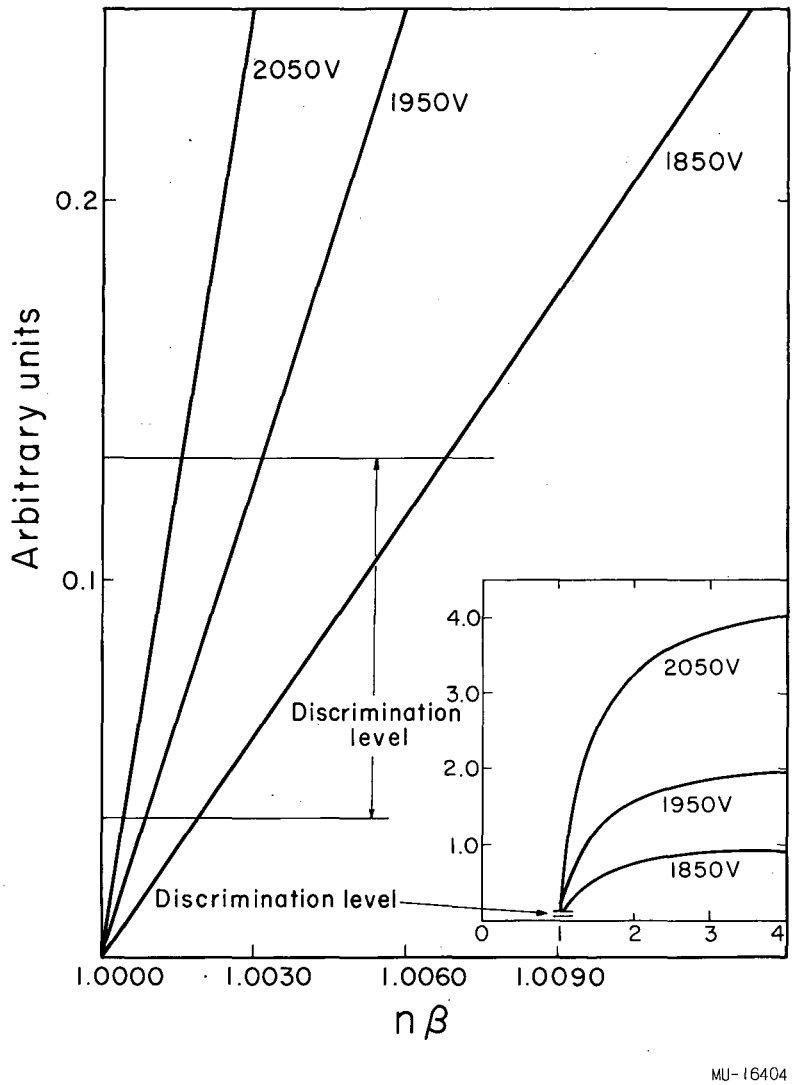

Fig. 9. Output voltage of phototube, $V_g - A_g [1 - (1/n^2\beta^2)]$ vs $n\beta$. The horizontal line corresponds to an output voltage of 2 v for a detection efficiency of 90%.

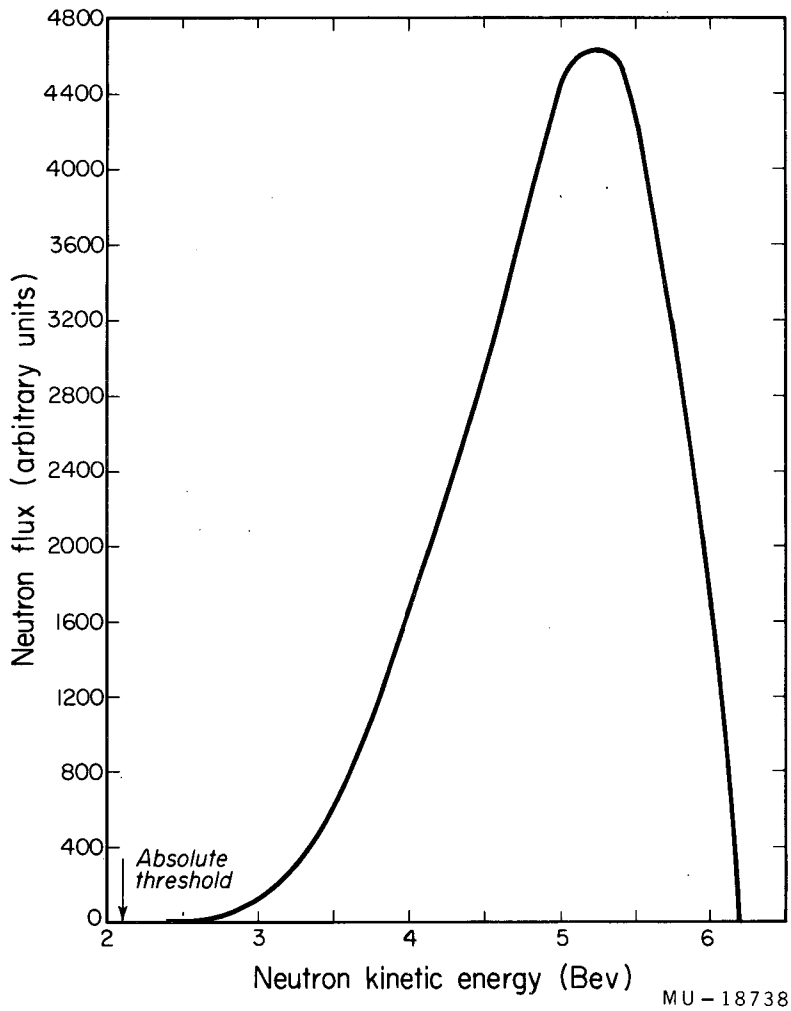

Fig. 10. Effective neutron-energy distribution. This distribution gives the most probable energy as $5.25 \pm^{.65}_{1.0}$ Bev and the mean energy as $5.0 \pm .4$ Bev, where the limits on the mean energy are the probable error points. The absolute energy range is 2.1 to 6.2 Bev.

of the spectrum the mean energy is 5.0 Bev with the probable error point at ±0.4 Bev. This distribution is derived by folding the primary neutron spectrum from the Bevatron, the energy distribution of pions from the converter for several pion-production multiplicities, and the energy-sensitivity curve of the Čerenkov counter together with appropriate weighting factors.

The primary beam spectrum of the neutrons coming from the Bevatron was measured by Holmquist[9] with a hydrogen diffusion cloud chamber. He got a distribution peaked at 3.8 Bev and going to zero flux at 6.2 and 1.4 Bev. Holmquist suggested that the data could be fitted with a smooth curve. A parabola fits his histogram quite well and was also convenient for calculation. This curve is given in Fig. 11. The validity of these assumptions is discussed in Section II. C. 2 (immediately following this section).

From the directional isobaric model proposed by Holmquist, the average percentages of 1π, 2π, 3π, and 4π events giving at least one charged pion may be deduced. The maximum pion energy available for different pion multiplicities and various incoming neutron energies may be easily calculated by using the Relativistic Kinematics Program for the IBM 650 developed by Lester K. Goodwin and Walton A. Perkins. Again Holmquist's data were used to give the charged-pion energy distribution in the forward direction for the 1π, 2π, 3π, and 4π multiplicities for an average incoming neutron energy for each case. The histograms given by Holmquist for each multiplicity and an average neutron energy were fitted with the simplified curve given in Fig. 12a. This simplified form was then shifted up or down in energy with E_{max} of the distribution, as each incoming neutron energy gives an E_{max} for each multiplicity different from the maximum pion energy resulting from the average neutron energy deduced by Holmquist.

As the Čerenkov counter threshold efficiency is the principal determining factor of the effective neutron distribution, this threshold effect must now be folded in. For a given neutron energy and a single pion multiplicity the effect of the Čerenkov counter threshold is

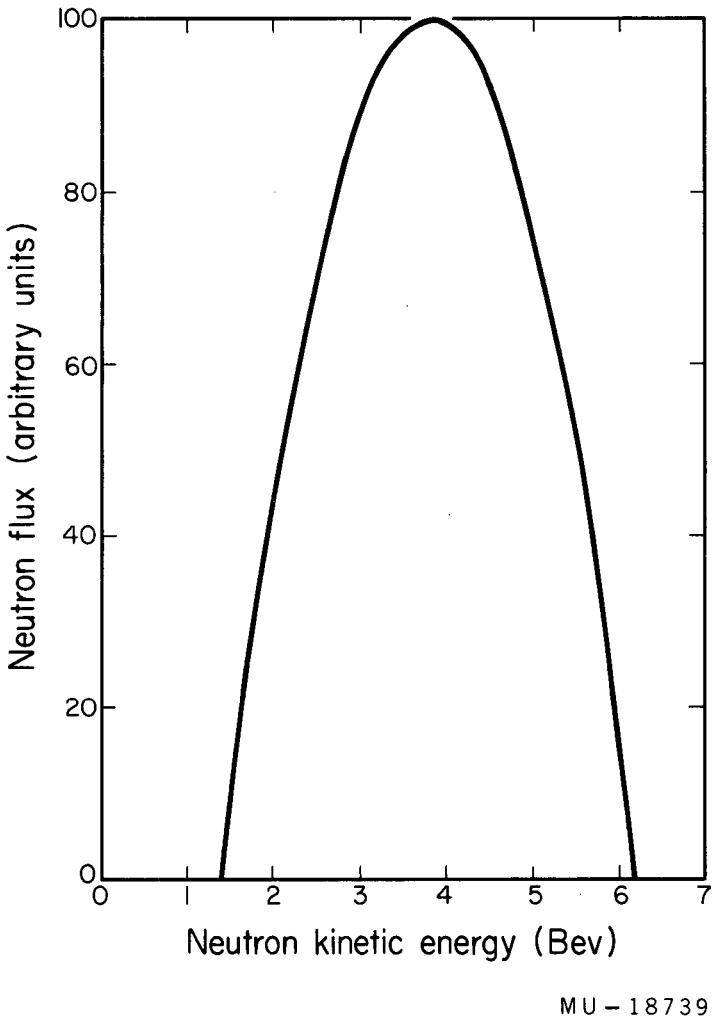

Fig. 11. Neutron-energy spectrum from the Bevatron target as measured by Holmquist.

illustrated in Fig. 12b. Only those pions represented by the area to the right of the dashed line representing the threshold curve of the counter are counted. Since the measured threshold-efficiency curves of the counter are essentially linear between the 10% and 90% efficiency points and are quite steep, taking the 50% efficiency point as the location of a threshold step function gives little error in the number of pions counted. This effective threshold is illustrated by the vertical solid line in Fig. 12b. However, the pion energy at the Čerenkov counter is degraded 100 Mev by the ionization energy losses in leaving the converter and passing through the electron filter. Thus the vertical line in Fig. 12b should be displaced 100 Mev to the right. The effective relative number of pions counting in the Čerenkov counter is given by the cross-hatched area of Fig. 12c.

All the above factors must now be folded together to give the effective neutron distribution. For each incoming neutron energy take:

a. The initial number of neutrons, $N_0(E)$, from Fig. 11
b. The percentage weight of each pion multiplicity case, M_i, and
c. The percentage of these pions produced above threshold, A_i, sum over the pion multiplicity cases, and combine:

$$N(E) = N_0(E) \sum_{i=1}^{4} M_i A_i \, . \qquad (3)$$

The percentage of pions produced above threshold is given by the ratio of the area in Fig. 12c to the right of the vertical line--the cross hatched area--to the total area of the simplified distribution. Only for incoming neutrons above 6.0 Bev energy are all pions counted for all pion multiplicities.

2. Assumptions

The assumptions and the models used in deriving this energy distribution are admittedly crude. Fortunately the mean effective neutron energy, which is the parameter of importance to the cross-

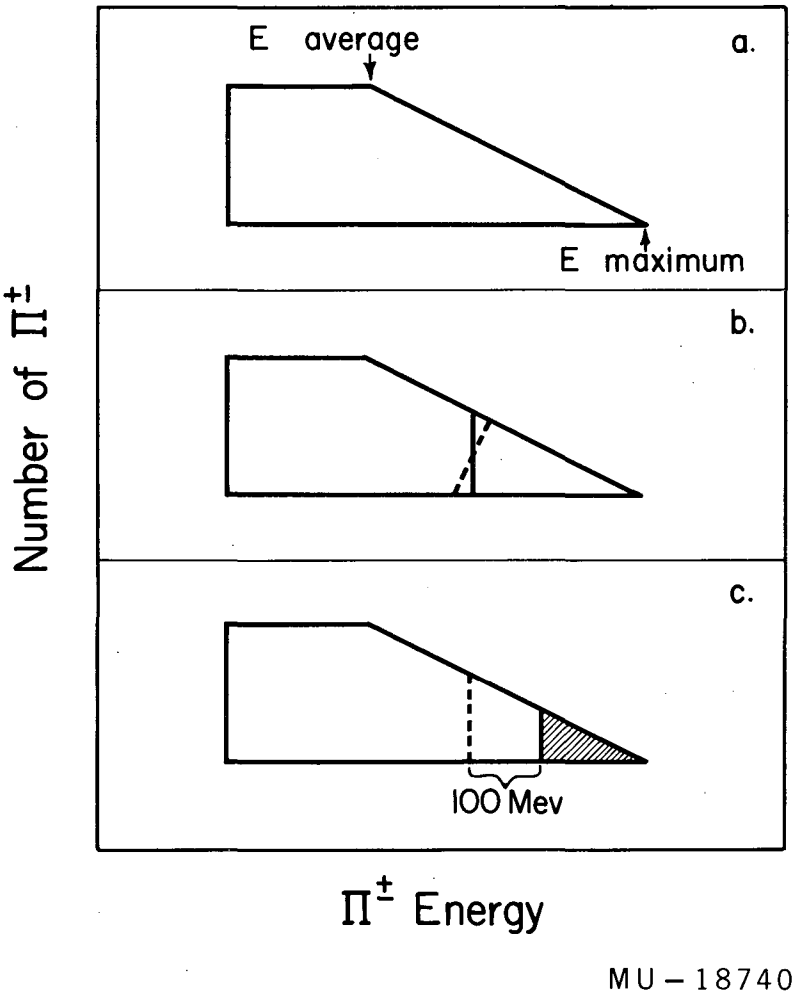

Fig. 12. Simplified pion-energy spectrum used to derive the effective neutron-energy spectrum.

section measurement, is not very sensitive to this derivation, since the Cerenkov counter threshold is the determining factor in the energy selection. The mean energy derived in this way is the energy expected from a very rough consideration of the 6.2-Bev upper limit of the Bevatron energy and the 3.5-Bev lower limit of the Čerenkov counter threshold plus the increased efficiency of the Čerenkov counter at higher energies.

Holmquist deduced the primary neutron energy spectrum from conservation of momentum and energy in his cloud chamber pictures. His peak energy and the fall-off of the energy distribution from its peak to zero at the maximum Bevatron energy of 6.2 Bev are corroborated by the work of Barrett with Bevatron neutrons in emulsion.[10] The symmetric drop of the neutron distribution to zero at 1.4 Bev is much more questionable, and may result from bias in the detection, scanning, and measuring methods used by Holmquist. However, because of the high effective threshold of the gas Čerenkov counter, the contribution to our effective distribution from neutrons below 3.8 Bev in energy is small.

At 5 Bev, nucleon-nucleon collisions were responsible for all pion production, since the binding energies and Fermi momenta of the nucleons in the beryllium nucleus are small by comparison. The assumption of charge independence permits the use of n-p data even though beryllium also contains neutrons. The angular dependence and energy dependence of the pion production were ignored, since there was not enough information available to permit these effects to be taken into account. However, these omissions are not too serious, since the angular distributions given by Holmquist are strongly peaked forward and backward in the center-of-mass system for the smaller pion multiplicities. Although the pion angular distribution is more isotropic for large pion multiplicities, there are then more pions produced, only one of which must pass through the gas Čerenkov counter to register a count. Also, the energies of the pions (in the laboratory frame of reference are near the mean, and again the

Čerenkov counter sees primarily the most energetic pion passing through it.

The simplified pion energy distributions used for this determination of effective neutron energy fit Holmquist's histograms of the pion-energy distribution quite well. These histograms are quite sketchy because of the very limited statistics available from a cloud chamber experiment. Probable alternate fits to these histograms do not make a significant change in the effective neutron energy distribution. The shifting procedure used to obtain points at a variety of energies is likewise justified on the basis that the final result is insensitive to the details of the pion energy distribution. Finally, a completely independent determination of the mean energy from the optical model of the nucleus is discussed in Section IV B. 4, which gives the same mean energy.

D. Counting Rates

The counting rates in this experiment were quite low, and were the limiting factor in both the accuracy and the extent of the experiment. The neutron counting rate with no absorber averaged 10 counts per minute, but varied from 1 to 100 counts per minute depending on the Bevatron beam levels and target configurations. The monitor counted at a rate approximately 100 times that of the neutron detector.

1. Neutron Production in the Bevatron Target

Barrett[10] measured the neutron reaction cross sections in lead, copper, and aluminum at the Bevatron with nuclear emulsions.[10] He calculated the source strength of the neutrons as 0.19 neutron per steradian per proton striking the target. His average neutron energy was calculated as 3.6 ± .7 Bev. He was unable to unfold the available data to get a neutron energy spectrum. His internal Bevatron target was 1 in. of polyethylene, and thus presented a lower density of nucleons to the circulating proton beam than the more substantial copper targets used in this experiment. However, because of multiple traversals of

the target by the circulating proton beam, this substantial difference in targets is probably unimportant. The difference in energy sensitivity of the detectors used is considered later.

The Brookhaven neutron experiment of Coor et al.[1] gave a neutron flux of 10^3 neutron per 10^{10} protons impinging on the target into a solid angle of 2.99×10^{-7} steradian.[1] This gives 0.34 n/steradian/proton. However, their energy "bite" was quite large, with their mean energy at 1.4 Bev and the effective cutoff points at 2.2 and 0.800 Bev. Their internal Cosmotron target was 6 in. of beryllium, and was quite effective in producing high-energy neutrons.

2. Attenuation and Solid Angle

The neutron beam, in leaving the Bevatron through the north straight section, passes through some steel supporting structure and then obliquely through the 1-in.-thick steel face plate of the straight section. In passing through these structures, the neutron beam has approximately a 4-in. path in steel. Estimating the neutron total cross section in iron by extrapolating our measured cross section for copper, we find the transmission of 4 in. of iron for 5-Bev neutrons is 0.440.

The 2 in. of lead in the gamma-ray filter in the entrance to the collimator also attenuates the neutron beam. Using our measured values for the total cross section of 5-Bev neutrons in lead, we find the undeflected transmission of the gamma-ray filter for neutrons is 0.680. Thus the total transmission constant for the primary neutron beam is 0.299, and 70% of the beam is lost before it reaches our absorbers or detector.

The neutron beam is very well collimated, since it is defined by the 2X2-in. converter and the 2X2-in. scintillation counter located immediately behind the converter, and the center of the converter is 86 feet from the primary neutron source at the Bevatron target. (The effect of secondary sources of scattered neutrons is shown in Section III.B2 to be negligible.) This excellent collimation is necessary, since the minima of the diffraction patterns for the elements being measured

occur at angles of the order of 1 deg. Thus unavoidably the very small solid angle of 3.76×10^{-6} steradian subtended by the detector at the Bevatron target greatly reduces the counting rate.

3. Detector Efficiency

The detection of high-energy neutrons is inherently inefficient, since the usual charged-particle detection methods depend on electromagnetic interactions, and the neutron magnetic moment is much too small to give useful coupling to the detector. Thus it is necessary to convert the neutrons to charged particles for effective detection. Detection efficiencies of about 0.1% are usual for processes of this type.

The beryllium converter used for this experiment has a maximum efficiency for converting neutrons to pions of 0.384 if the rather ideal circumstances given in Section II. C. 2 are met. This assumes that every neutron that interacts inelastically in the converter produces pions which go forward in the laboratory system within the 3-deg cone subtended by the gas Čerenkov counter. Most of the neutron inelastic collisions produce pions at this high neutron energy. An examination of the angular distributions of pions produced in high-energy n-p scattering given by Holmquist[9] suggests an estimate of 0.25 for the proportion of pions produced in a 3-deg cone about the forward direction. Finally, the directional isobar model of Holmquist indicates that in 1/3 of the inelastic neutron collisions, only neutral pions are produced; these are of course undetected. Thus the total efficiency to this point is given by

$$\text{Eff.} = 0.67 \times .250 \times .38 = .064$$

The 2 in. of lead and 1 in. of iron in the electron filter that follows the converter also absorb pions. Interpolating the pion total cross sections for Pb and iron from the 4.2-Bev π^- cross-section data of Wikner,[11] one finds the pion transmission of the iron is approximately 0.787 and of the lead 0.566. This gives a total undeflected pion transmission for the electron filter of 0.445.

A price must also be paid for the energy-selection characteristics of the gas Čerenkov counter, since it counts only high-energy pions with good efficiency. The fraction of available neutron energy spectrum detected by our neutron detector is given by the ratio of the normalized area of our neutron energy distribution (Fig. 10) to the area of the primary neutron energy distribution from the Bevatron (Fig. 11) as measured by Holmquist. The energy-selection characteristics of our detector thus give a factor of 0.160 in the total detector efficiency. Hence the total counting efficiency of the detector is given by

$$\text{Eff.} = 0.160 \times 0.445 \times 0.064 = 4.6 \times 10^{-3}.$$

4. Total Counting Rate

Our neutron counting rates should now be directly comparable with those measured by Barrett. Using Barrett's neutron production rate and considering the attenuation of the beam, the solid angle subtended by our detector, and the efficiency of our detector, we predict a counting rate of

$$0.19 \times 0.299 \times 3.76 \times 10^{-6} \times 4.55 \times 10^{-3} = 9.73 \times 10^{-10}$$

neutron counts per proton on the target. Thus we would expect a counting rate of 10 counts per 10^{10} protons on the target.

An adjustment must be made to the Brookhaven counting-rate data of Coor et al.,[1] since they used a relatively wider energy bin. The relative energy bites may be taken as the energy spread divided by the mean energy. The relative energy bite for this experiment, then, is

$$\frac{6.2 - 3.4}{5.0} = 0.56,$$

whereas that for the Brookhaven experiment is

$$\frac{2.20 - .54}{1.4} = 1.15$$

Thus a factor of 0.487 (i.e., 0.56/1.15) must be inserted to compare our counting rates with those of the Brookhaven experiment. Now,

our counting rate may be predicted from the Brookhaven data, giving $0.487 \times 0.335 \times 0.299 \times 3.76 \times 10^{-6} \times 4.55 \times 10^{-3} = 8.36 \times 10^{-10}$ neutron counts per proton on the target, or 8 neutron counts per 10^{10} protons.

These predicted counting rates agree within an order of magnitude with the observed counting rate. Since this experiment used proton beams scattered from other targets, it was difficult to know the number of protons striking the neutron-producing target. This comparison of counting rates indicates that this symbiotic mode of operation is about 10% efficient, since we typically got one neutron count per 10^{10} protons in the circulating beam.

5. Monitor Counting Rate

The monitor counting rate is chosen, for statistical reasons, to be approximately 100 times the neutron counting rate. Since the monitor primarily sees charged particles produced in the lead gamma-ray filter and in the walls of the collimator by neutral particles, it subtends a much larger solid angle than the neutron detector. The monitor energy sensitivity may be selected by adjusting the gas pressure in the monitor Čerenkov counter, and should be comparable to the energy sensitivity of the neutron detector. The monitor Čerenkov counter normally operated at 2/3 the absolute pressure of the neutron Čerenkov counter. This not only gave improved tracking of the monitor with the neutron detector, but also gave desirable relative counting rates. The monitor counting rate could also be adjusted by changing the amount of material producing charged particles immediately ahead of the monitor.

III. RESULTS

A. Cross-Section Measurements

1. Transmission Measurement

This experiment was basically a simple transmission measurement. The transmission of various absorber thicknesses was measured in good geometry (~0.2 deg) and poor geometry (~4 deg). For lead and carbon the integrated cross section was also measured as a function of the half angle subtended by the detector (converter). The angles of the first diffraction minima vary with element from 1 to 2 deg, making all the angles of interest quite small. The angles of the first diffraction minima for the elements measured are given in Table I. This angle is calculated on the opaque circular cylinder model, which gives

$$\theta_m = 0.61 \frac{\lambda}{R} = 0.61 \frac{h}{pR} ,$$

where θ_m is the half angle of the first minimum, λ is the wave length of the scattering particle, and R is the radius of the scattering nucleus. The two absorber thicknesses used were generally 0 and approximately a half absorption length in the element being measured. These lengths gave an appreciable transmission difference while minimizing multiple-scattering problems. The number of neutrons transmitted is given by

$$N = N_0 \; e^{-n\sigma x} ,$$

where N is the number of neutrons transmitted, N_0 is the number of neutrons in the incident beam, n is the number of nuclei per unit volume in the absorber, σ is the neutron cross section of the absorber element, and x is the absorber thickness. The measured neutron-detector counts per thousand monitor counts are given by

$$R = C \frac{N}{N_0} = C \, e^{-n\sigma x} ,$$

where C is a constant which relates the number of neutrons in the unattenuated beam to the number of monitor counts.

Table I

Positions of Diffraction Minima

	First minimum		Positions (deg) at which cross sections were measured	
	$\sin\theta$	θ	σ_r	σ_t
Pb	0.0186	$1^\circ 4'$	4°	0.184°
Sn	0.0224	$1^\circ 17'$		
Cu	0.0276	$1^\circ 35'$	5°	0.208°
Al	0.0366	$2^\circ 6'$	5°	
C	0.0479	$2^\circ 45'$	7°	0.209°
H	0.1095	$6^\circ 17'$	$\sim$	0.25°

The slope of a semilog plot of ln R versus x now gives σ directly, since we have

$$\ln R = n\sigma x + \ln C,$$

and the value of C need be constant only for runs with at least two thicknesses. A least-squares fit is made to the rate data for various thicknesses of an element. The slope $b = \sigma n$ is given by

$$a = \frac{\sum_i w_i \sum w_i x_i y_i - \sum_i w_i x_i \sum w_i y_i}{D},$$

$$D = \sum_i w_i \sum_i w_i x_i^2 - \left(\sum_i w_i x_i\right)^2, \qquad (4)$$

where y equals ln R and w is the weight of each point. The sums are over the various thicknesses of absorber. Because of the change of variable, R to ln R, the weights are given by

$$W = \frac{1}{(\epsilon')^2},$$

where ϵ' is the percentage error, $\mathcal{E}/R$. The error on the slope is given by

$$\epsilon_b = \sqrt{\frac{\sum w_i}{D}}. \qquad (5)$$

The data illustrated in Fig. 13 for several thicknesses of lead are fitted well by a straight line. Since some of these thicknesses are substantially greater than a half absorption length, this good fit indicates that we are truly measuring an exponential decrease.

2. Geometric Corrections

Since the angles related to the diffraction pattern are small (as discussed above), the diffraction pattern is seriously smeared out by the 2X2-in. finite size of the neutron beam. The finite sizes of the beam and of the converter make the definition of the angle subtended by the detector indefinite, particularly for the poor-geometry measurements. For example, compare the angles θ and θ' in

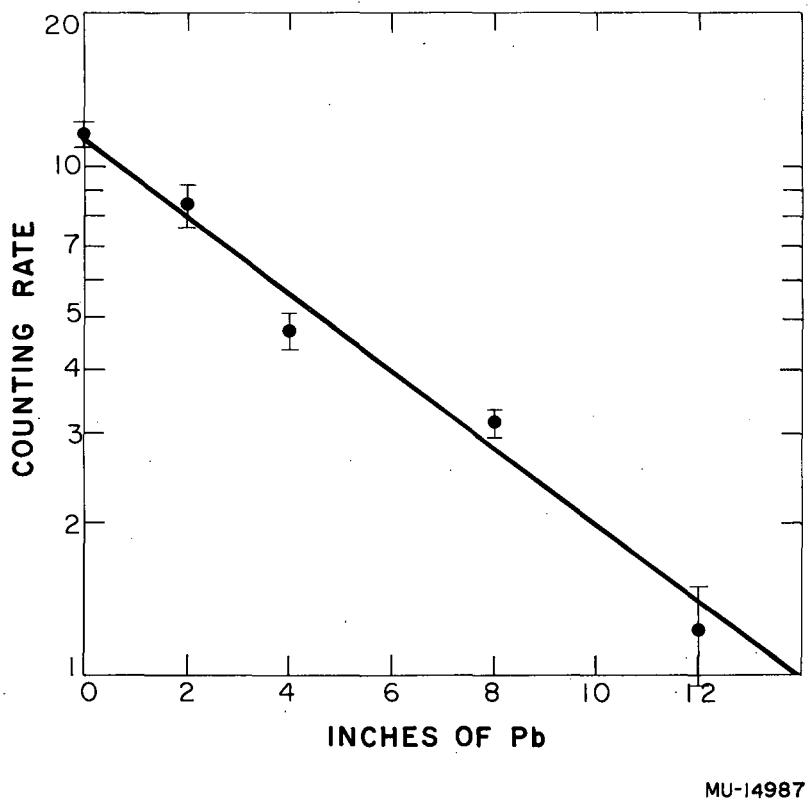

Fig. 13. Counting rate vs thickness of lead absorber, showing the exponential decay, the slope of which gives the cross section.

Fig. 14, where the areas A_1 and A_2 represent the midsections of the absorber and the converter respectively and the neutron beam is proceeding along the Z axis.

A geometric correction for the finite beam size was made as follows: The diffraction pattern for an opaque cylinder is given by

$$\frac{d\sigma_d}{d\Omega} \sim \left[\frac{J_1 (kR \sin \theta}{\sin \theta} \right]^2 , \qquad (6)$$

where $\frac{d\sigma_d}{d\Omega}$ is the differential elastic-scattering cross section, J_1 is the first-order Bessel function, and k is the neutron wave number. This is close to the scattering from an opaque sphere for $KR > 1$, where K is the absorption constant of the optical model discussed in Section IV.C. Values of KR for this experiment range from 2.98 for lead to 1.16 for carbon.

The partially integrated elastic-scattering cross section is defined as

$$\sigma_d (\theta) = \int_0^\theta \frac{d\sigma_d}{d\Omega} \, d\Omega . \qquad (7)$$

A mean $\sigma_d (\theta)$ for a finite beam size may be defined as

$$\overline{\sigma_d (\theta)} = k \int_{A_1} \int_{A_2} \left[\frac{J_1 (k R \sin \theta)}{\sin \theta} \right]^2 \times \frac{dA_1}{\ell 2} \frac{dA_2}{A_2} . \qquad (8)$$

Normalize $\overline{\sigma_d (\infty)} = 1$, and define the partially integrated differential cross section normalized to unity as

$$F (\theta) = \frac{1}{\sigma_d} \int_0^\theta \frac{d\sigma_d}{d\Omega} \, d\Omega . \qquad (9)$$

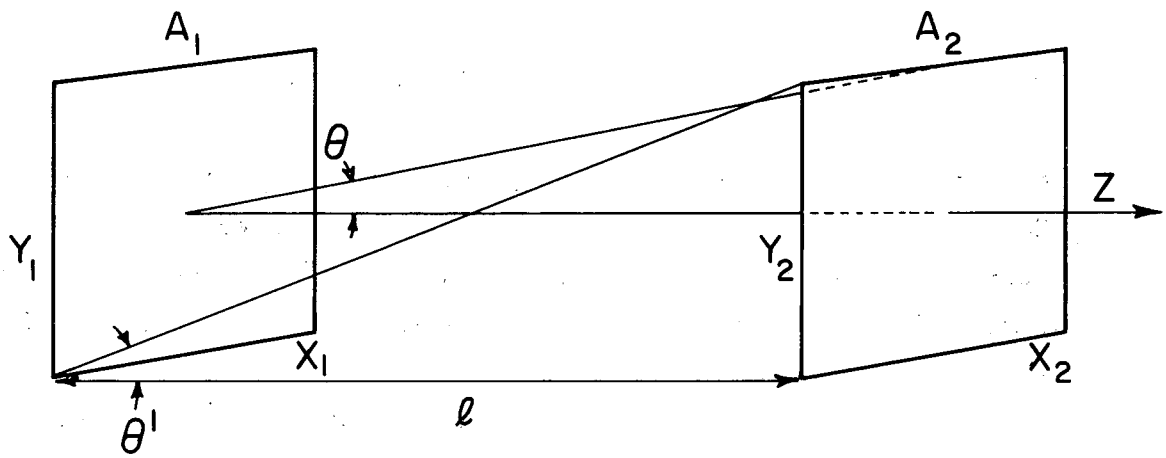

MU-18741

Fig. 14. Simplified diagram showing the geometry of the absorber and converter.

Then $\sigma(\theta)$, the cross section determined by the transmission at a given subtended angle θ, is related to the reaction cross section σ_r and elastic cross section σ_d by:

$$\sigma(\theta) = \sigma_r + \left[1 - F(\theta)\right] \sigma_d \tag{10}$$

$$= \sigma_r + F'(\theta)\ \sigma_d .$$

Now $\sigma(\theta)$ is measured by this experiment for several values of θ. $F(\theta)$ has been calculated by a machine (IBM 650) evaluation of Eq. (6). Then a least-squares fit of the linear form of Eq. (10) gives σ_r as the intercept (a) and σ_d as the slope (b) of the straight line. The forms for computing b and $\mathcal{E}_b$ were given in Eqs. (4) and (5), and the forms for a and $\mathcal{E}_a$ are

$$b = \frac{\sum_i w_i x_i^2 \sum_i w_i y_i - \sum_i w_i x_i \sum w_i x_i y_i}{D}$$

$$\mathcal{E}_a = \sqrt{\frac{\sum_i w_i y_i}{D}} , \tag{11}$$

where $X = F'(\theta)$, $Y = \sigma(\theta)$, $W = \frac{1}{\mathcal{E}^2}$, and the sums are over the various values of θ. The corrections for the finite beam size raise the total cross section as much as 5% for lead and decrease the reaction cross section as much as 10% for carbon.

The above correction assumed that all scattered neutrons were scattered at the midplane of the absorber and produced pions in the midplane of the converter. A small correction was made for this by integrating along the beam (Z) direction also. The finite length of the absorber again makes θ, the angle subtended by the detector, indeterminate. However, this effect averages out, since sin θ is linear for the small angles involved. The converter efficiency (W)

varies slowly with length and is given by

$$W = [\exp(-Z/\lambda_n) - \exp(-Z/\lambda_\pi)] / [(\lambda_\pi \lambda_n) - 1],$$

where λ_n is the inelastic interaction length for neutrons in beryllium and λ_π is the total interaction length for pions in beryllium. The sensitivity of the detector is assumed to be constant for the scattering angles possible in this experiment. Since the Čerenkov counter accepts less than a 3-deg cone, the pion angular distribution is flat over these small angles, as is indicated in the Holmquist[9] and Brookhaven[1] papers. There is some indication in the data that for the largest angle measured for carbon this assumption is breaking down.

3. Results

The results of all the transmission measurements for all angles measured and for all elements measured are given in Table II. Table III gives the total cross section (σ_t), reaction cross section (σ_r), and elastic cross section (σ_d) derived from these measurements, and compares them with two commonly used geometric cross sections. Figures 15 through 18 illustrate the corrected least-squares fits to the experimental data.

Table II

Measured cross sections, $\sigma \pm \epsilon$ (in mb)

L in.	θ deg	Pb	Sn	Cu	Al	C	H
320	.179	2445 ± 257					
312	.184	2325 ± 131				324 ± 20.2	
308	.186						
276	.208	2445 ± 82	1986 ± 87.5	1097 ± 28.1	601 ± 29.8		
275	.209					302 ± 19.9	
232	.248						33.6 ± 1.6
114.5	.500	1948 ± 141					
57.25	1.00	1760 ± 147					
36.0	1.59					292 ± 18	
28.5	2.00	1860 ± 224					
23.65	2.42	1684 ± 360					
14.5	3.95					240 ± 14.9	
14.0	4.1	1744 ± 120					
11.5	5.0			594 ± 24.5	436 ± 77.7		
9.5	6.0				380 ± 28.4		
8.94	6.38	1720 ± 208					
8.0	7.13					268 ± 31.3	
6.5	9.6	1725 ± 197					

Table III

Measured total, reaction, and elastic cross section, and two common geometric cross sections for various elements (in mb)

Element	σ_t	σ_r	σ_d	$20\pi A^{2/3}$	$1.28\ A^{1/3}$
Pb	2534 ± 105	1670 ± 79	864 ± 131	2190	1802
Sn	1986 ± 88			--	--
Cu	1158 ± 34	586 ± 25	572 ± 42	1000	817
Al	614 ± 33	381 ± 27	233 ± 43	560	414
C	319 ± 20	235 ± 16	83.6 ± 25.6	330	271
H	33.6 ± 1.6			60	51.9

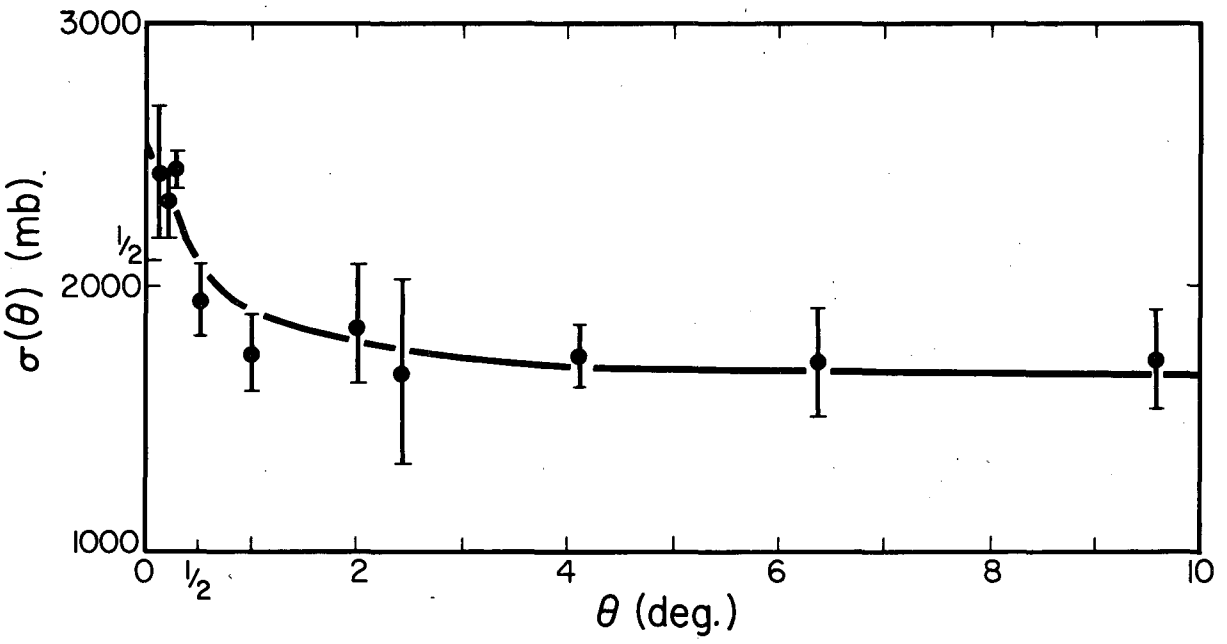

MU-18742

Fig. 15. Cross section of neutrons in lead as a function of the half angle subtended by the neutron detector. The solid curve is a least-squares fit to the data according to an opaque-nucleus calculation for a mean neutron energy of 5.0.

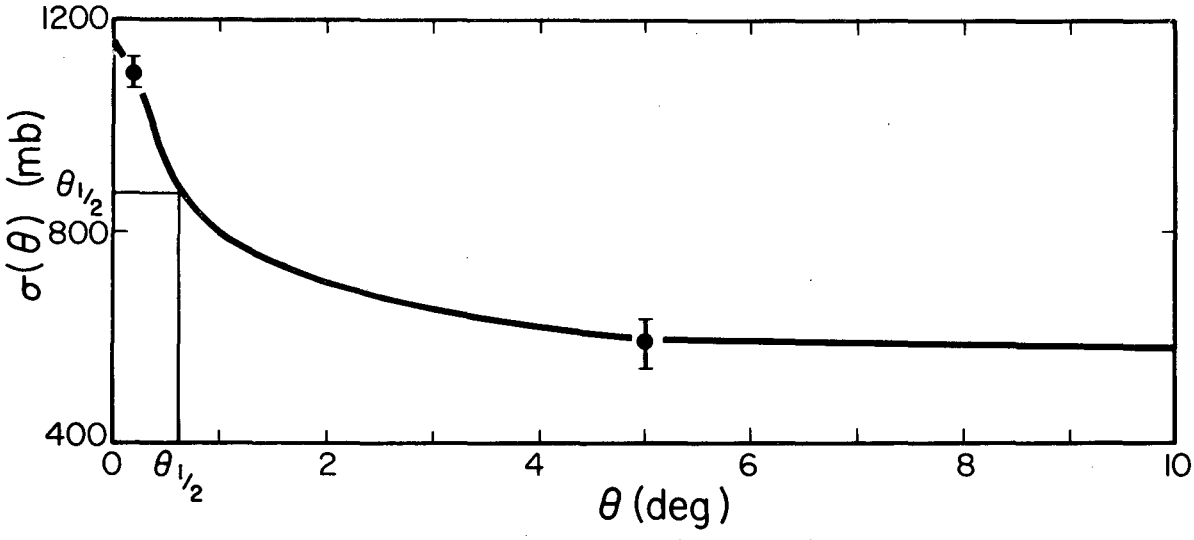

MU-18794

Fig. 16. Cross section of neutrons in copper as a function of the half angle subtended by the neutron detector. The solid curve is a least-squares fit to the data according to an opaque-nucleus calculation for a mean neutron energy of 5.0 Bev.

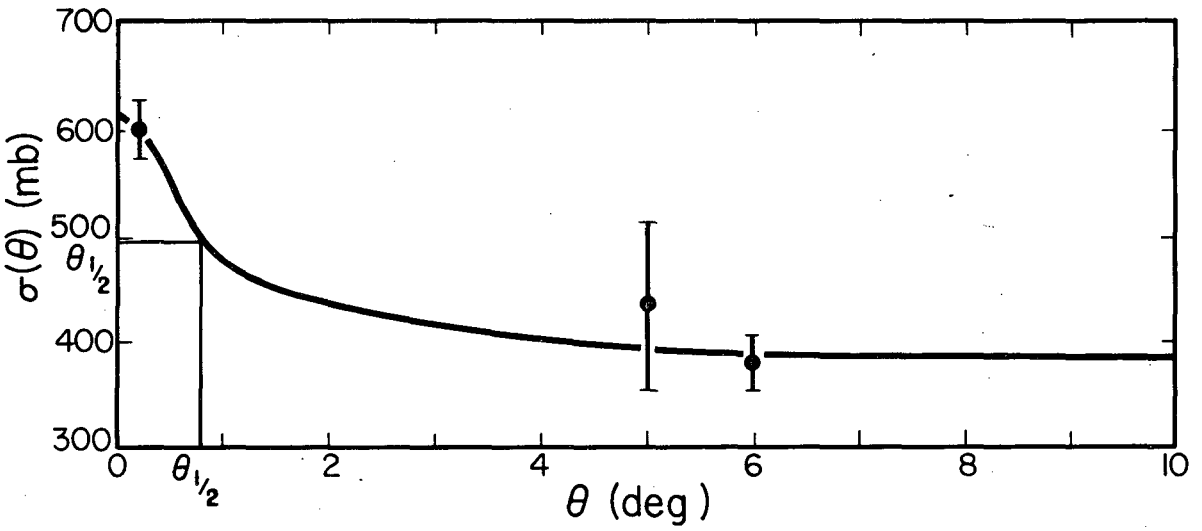

MU-18795

Fig. 17. Cross section of neutrons in aluminum as a function of the half angle subtended by the neutron detector. The solid curve is a least-squares fit to the data according to an opaque-nucleus calculation for a mean neutron energy of 5.0 Bev.

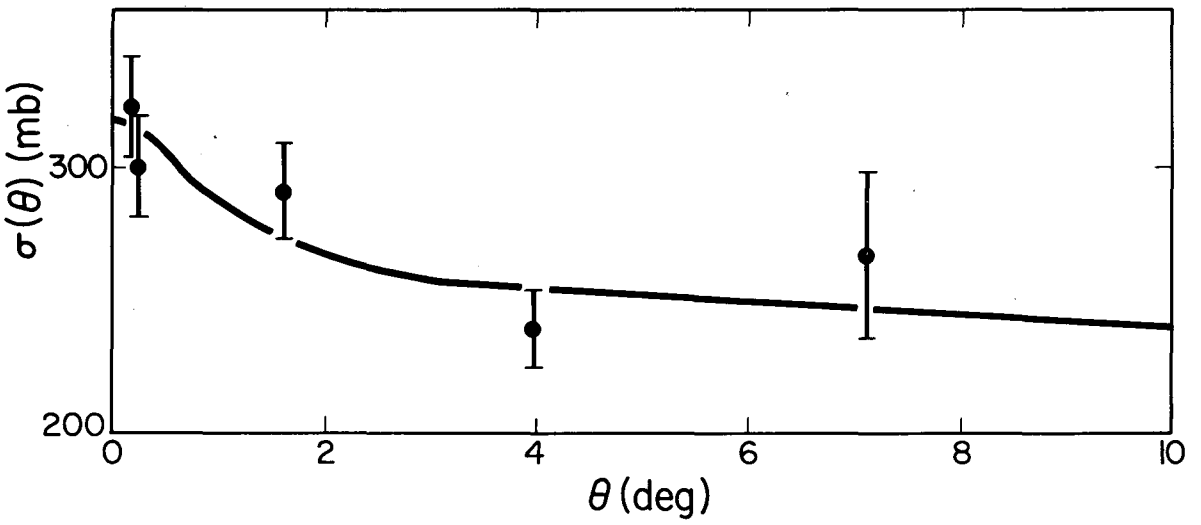

MU-18743

Fig. 18. Cross section of neutrons in carbon as a function of the half angle subtended by the neutron detector. The solid curve is a least-squares fit to the data according to an opaque-nucleus calculation for a mean neutron energy of 5.0 Bev.

B. Errors

1. Beam Contamination

Contamination of the neutron beam with charged particles or other neutral particles could give errors in the cross-section measurements. But charged particles generated in the Bevatron target are swept out by the Bevatron magnetic field before reaching the collimator. No charged-particle orbits were found with an automatic orbit plotter (bug) which originated at the 72-deg target and passed through the collimator. Scattered charged particles are further deflected into the walls of the 5-ft-long lead collimator by the 1000-gauss stray field from the Bevatron at the collimator position. Measurements with the monitor counter telescope and calculations of the neutron-detection efficiency indicate that the beam consists of less than 10% charged particles at the monitor position. Comparison of the neutron counting rates with the anti-counter on and off indicates that the ratio of charged to neutral particles at the detector is less than 2×10^{-4}. To affect the cross-section measurements adversely, charged particles must produce neutrons in the absorber, since the anti-counter effectively removes charged particles, as does the subtraction of background counting rates with converter out. Thus the effects of charged-particle contamination are negligible.

High-energy gamma rays are produced in the Bevatron target in numbers comparable to the number of neutrons produced. However, they must pass through 4 in. of steel and 2 in. of lead before reaching the monitor counters. This is 16 radiation lengths of material and greatly degrades both the number and energy of the gamma rays. Further, to introduce a serious error the gammas must produce neutrons in the absorber or charged pions in the converter, since an effective electron–gamma-ray filter follows the converter. These are unlikely processes, and gamma rays were not a problem. Neutral pions likewise decay virtually immediately into two gamma rays and are eliminated.

All the neutral strange particles, with the exception of the long-lived component of the neutral K particles, have lifetimes shorter than 10^{-10} second and cannot traverse the 86-ft path length of this experiment. The K_2^o has a mean life of approximately 10^{-7} sec and could possibly cause trouble. However, K^o mesons are produced at only about 10^{-4} the rate of neutrons in the Bevatron target.[12] Half of those produced decay quickly by the K_1^o mode, and the K_2^o mode regenerates K_1^o -mode particles in interactions in the 4-in. of steel and 2-in. of Pb in the beam, further reducing the K^o flux by decay through the K_1^o mode. Finally, K^o mesons do not have radically different cross sections than neutrons, making very small contaminations unimportant. Thus beam contamination does not introduce errors within the accuracy of this experiment.

2. Geometry

Because of the very small angles involved in this experiment, geometric corrections or errors can be very important. The geometry of the primary neutron beam is well defined, since the distances are large between the target and the relatively small detector elements. The neutron beam is defined to a half angle of 0.114 deg by the collimator, 0.152 deg by the monitor, and 0.0556 deg by the neutron detector (converter). However, the lead gamma-ray filter in the mouth of the collimator acts as a diffuse source of elastically scattered neutrons.

Elastically scattered neutrons from the 2-in. lead gamma-ray filter comprise 20% of the neutron beam on the basis of our measured value of σ_d. The gamma-ray filter is 18 ft from the good-geometry absorber position and the absorber subtends an angle of 0.53 deg. Since the diffraction-pattern minimum for elastically scattered neutrons from lead is at 1 deg, approximately 75% of the neutrons are scattered through angles less than 0.53 deg. Half of these neutrons scatter toward the central ray and thus possibly into the neutron detector. The change in cross section resulting from a change in the subtended angle of the good-geometry position from 0.2 deg to 0.5 deg may be estimated (from the variation of integral cross section as a function

of angle, illustrated in Fig. 15) as 20%. These factors are now combined:

$$0.20 \times 0.75 \times 0.50 \times 0.20 = 0.015.$$

This maximum error estimate of 1.5% indicates that this error is not significant in comparison with the statistical uncertainties of the experiment.

Corrections for the alteration of the diffraction pattern by the finite beam size were made in Section III. A. 2. Since these corrections are a maximum of 10%, a 10% error in the model used for the correction would give a cross-section error of 1%. Since the model used applies well for $KR > 1$ and our values of KR range from 1.16 to 2.98, the error from this correction should be much less than 1%.

The effect of multiple scattering of the neutrons in the absorber is thoroughly discussed by Coor et al.[1] for a similar experiment on 1.4-Bev neutron cross sections performed at Brookhaven. Their corrections to the cross sections for this effect were less than 1/2%. Our corrections would be less than this, since the cross sections are smaller at our higher energy and the angles subtended by the detector are also smaller.

In poor geometry, neutrons from some inelastic events are also collected. This problem was considered by Cronin et al.[13] for a high energy pion scattering experiment. The cross section measured at a given subtended angle θ is given by

$$\sigma(\theta) = \sigma_r + F'(\theta)\,\sigma_d - \int_0^{\theta} \left[\frac{d\sigma_r(\theta)}{d\Omega}\right] d\Omega . \qquad (12)$$

This differs from Eq. (10) only by the subtraction of the last term, which is the correction for inelastic events counted.

The differential reaction cross section, which gives the number of high-energy neutrons inelastically scattered into unit solid angle, may be expanded in a cosine series as follows:

$$\left[\frac{d\sigma(\theta)}{d\Omega}\right]_r = \sum_n |a_n| \cos^n \theta . \qquad (13)$$

Then if the reaction cross section, σ_r, is extrapolated linearly from 7.5 deg and 15 deg the error is less than 2% when this is compared with the form of Eq. (13) for $n \leq 12$. The angles on which our values for σ_r are based are of the order of 4 deg, so the value of σ_r may be assumed to project linearly to 0 deg. The measured cross section may be given by an expansion of Eq. (12) as

$$\sigma(\theta) = \sigma_r + F'(\theta)\,\sigma_d - 2\pi\eta(1-\cos\theta),$$

where η is less than σ_r. Since cos 4 deg is 0.998, the correction is less than 0.2% even if all the inelastic events give high-energy neutrons in the forward hemisphere.

3. Bevatron Proton Beam Tracking

By far the largest error in the operation of this experiment came from tracking variations of the Bevatron internal proton beam. The ratio of neutron counts to monitor counts depended on the Bevatron target configuration and on the steering or tracking of the Bevatron internal proton beam. Unfortunately, the requirements of this experiment did not control the Bevatron operation conditions.

Variations in the ratio of neutron to monitor counts arise because the monitor is more sensitive to variations in the internal proton beam than the neutron detector. Both neutrons and charged particles are produced in the top and sides of the Bevatron vacuum tank as well as in the target. However, the neutron flux measured by the neutron detector is more target-sensitive than the monitor counting rate because of extreme collimation of the neutron flux at the detector. The use of a gas Čerenkov counter in the monitor limits the energy sensitivity of the monitor to high energies, at which the proton-beam fluctuations are smaller and most of the particles are produced in the target. Thus the gas Čerenkov counter reduces the variations in the ratio of neutron counts to monitor counts.

Fortunately the errors introduced in the measured rates by variations in Bevatron operating conditions are essentially random, since there is no correlation between the Bevatron beam condition and our

absorber and converter configurations discussed in Section II. A. 3. As the absorber and converter configurations are changed hourly, the variations in the measured rates average out with many runs. Also, only internally consistent rates are combined with one another to derive a cross section. The statistical criterion of Rossini and Deming,[14] was used to test consistency. This criterion requires that the plot of each point plus two standard deviations overlap the plot of the mean plus two standard deviations on the mean. Cross sections derived independently from each consistent set of rates are then combined if consistent to give the quoted cross section. The statistical considerations discussed in the next section (III. B. 4) establish that these procedures make the error from internal proton-beam variations much less than the counting-statistics error.

4. Counting Statistics and Total Error

The low counting rates, discussed in Section II. D, make counting statistics the chief limitation in the accuracy of this experiment. Because of the logarithmic relationship of the cross section to the measured counting rates, very good statistics, an error less than 1%, are needed on the measured rates to give an error in the cross section of less than 5%. Since there are no known systematic errors greater than 1%, the quoted errors are counting-statistics errors. The following statistical considerations indicate that this is a reasonable estimate to the total error of the experiment.

Most of the rate data and cross sections were sorted and combined as consistent data by using Eqs. (4) and (5) and the criterion of Rossini and Deming.[14] However, all the data were also combined using Eq. (4) for the mean and the following equation for the error:

$$\bar{\varepsilon} = \sqrt{\frac{\sum WX^2}{n\,\varepsilon\,\bar{W}}}\,, \tag{5b}$$

where $X = \sigma - \bar{\sigma}$, the deviation of the measured cross section from the mean cross-section, n is the number of measurements, and W is the weight as defined for Eq. (4). The means derived were the

same within the errors on each mean whether the data were all combined as inconsistent data or sorted for consistency. The use of sorted internally consistent data usually resulted in smaller errors. A comparison of the independently calculated cross sections with the normal distribution expected for the quoted error indicates that the data for most elements are grouped better than one would expect for a normal distribution. Thus the random rate variations due to Bevatron operating conditions discussed in the previous section (III. B. 3) do not affect the measured cross sections within the statistical accuracy of the experiment. For this reason the counting-statistics errors are quoted as the total statistical error. Since all known systematic errors were shown to be less than 1% in Sections III. B. 1, III. B. 2, and III. B. 3, the counting-statistics errors are used as an estimate of the total error.

IV. CONCLUSIONS

A. Discussion

1. Comparison with Previous Experiments

The striking variation with energy of the neutron total cross section for lead, copper, aluminum, and carbon is illustrated in Figs.19, 20, 21, and 22. The rise in the neutron total cross sections from 300 Mev to 1.5 Bev was established in 1955 by Coor et al. with their experiment at 1.4 Bev, and later data at lower energies confirm this behavior. Our values for the neutron total cross sections show a consistent and substantial drop from the Brookhaven values. The high-energy cosmic-ray values of Sinha and Das[15] for the total cross section of 4-Bev penetrating secondaries in aluminum, copper, and lead are somewhat lower than our values for neutron cross sections in the same elements. However, these cosmic-ray cross-section experiments are quite tenuous, since neither the energy nor the identity of the bombarding particles was well established.

The reaction cross section is essentially constant within the accuracy of the experiments from 300 Mev to 5 Bev for all the elements measured. This is confirmed by the Brookhaven 1.4-Bev data,[1] Barrett's data at 3.6 Bev,[10] and the cosmic-ray data at 4.0 Bev of Sinha and Das.[15] Thus the radical change in the total cross section must be due to a sharp drop in the elastic cross section. The theory developed in Section IV.B relates this decrease to a decrease in the nucleon-nucleon cross section.

2. Nucleon-Nucleon Cross Sections

The nucleon-nucleon cross section is of course one of the basic parameters of nuclear physics. Coor et al.[1] measured the n-p cross section by taking a CH_2-C attenuation difference. This technique required too much time with our low counting rates to get acceptable statistical accuracy. A liquid hydrogen target was used in this experiment to give the n-p cross section directly. The n-p total cross section exhibits the same drop from 1.4 to 5.0 Bev as was characteristic of the heavier nuclei discussed above. The high-energy

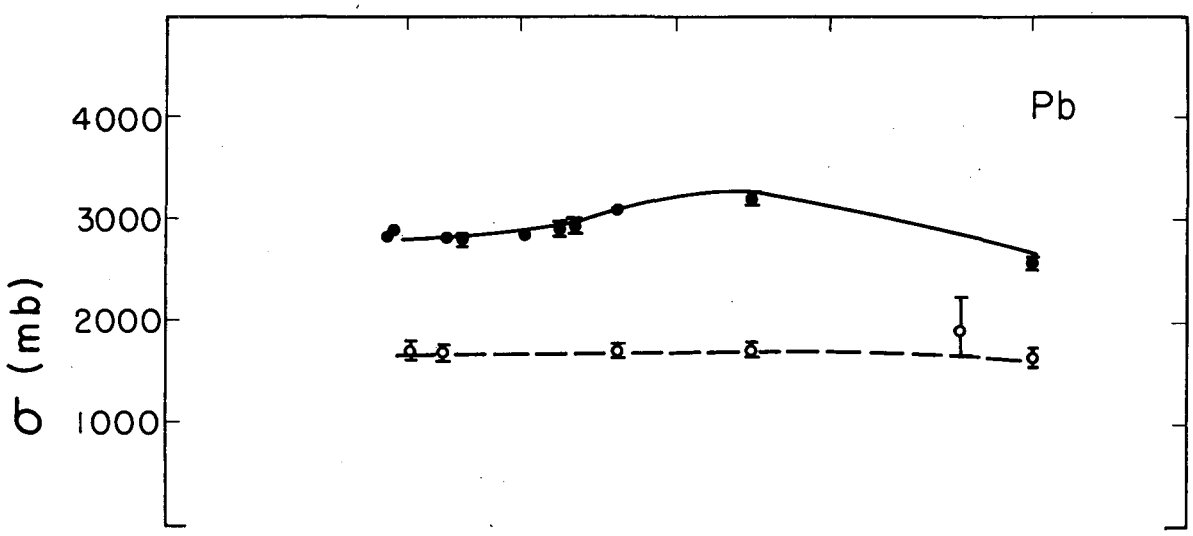

MU-18802

Fig. 19. Neutron total and reaction cross sections for lead. The solid curves are the theoretical total cross sections and the dashed curves are the theoretical reaction cross sections. The circles are the experimental measurements.

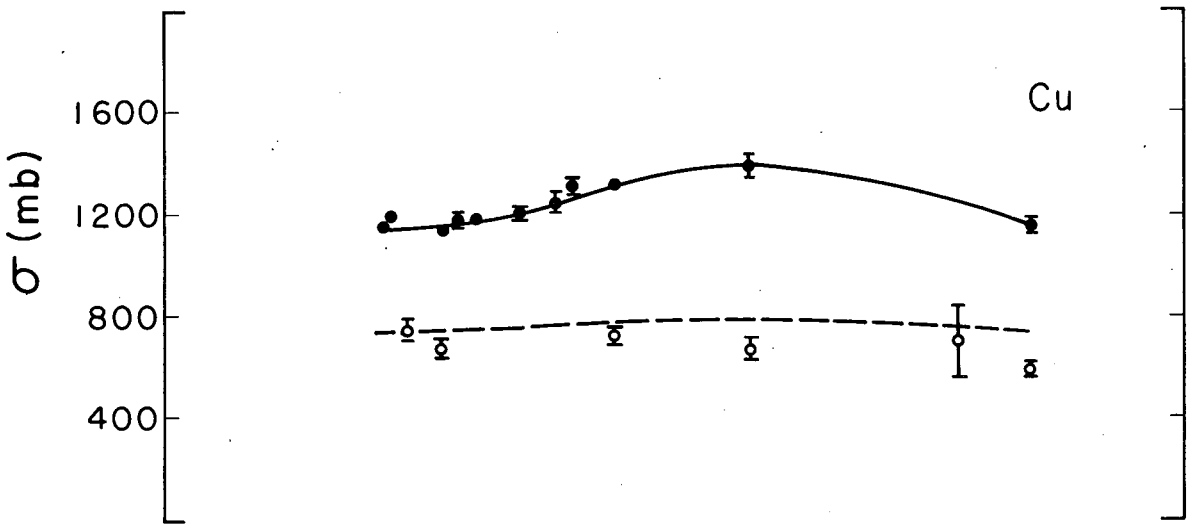

MU-18801

Fig. 20. Neutron total and reaction cross sections for copper. The solid curves are the theoretical total cross sections and the dashed curves are the theoretical reaction cross sections. The circles are the experimental measurements.

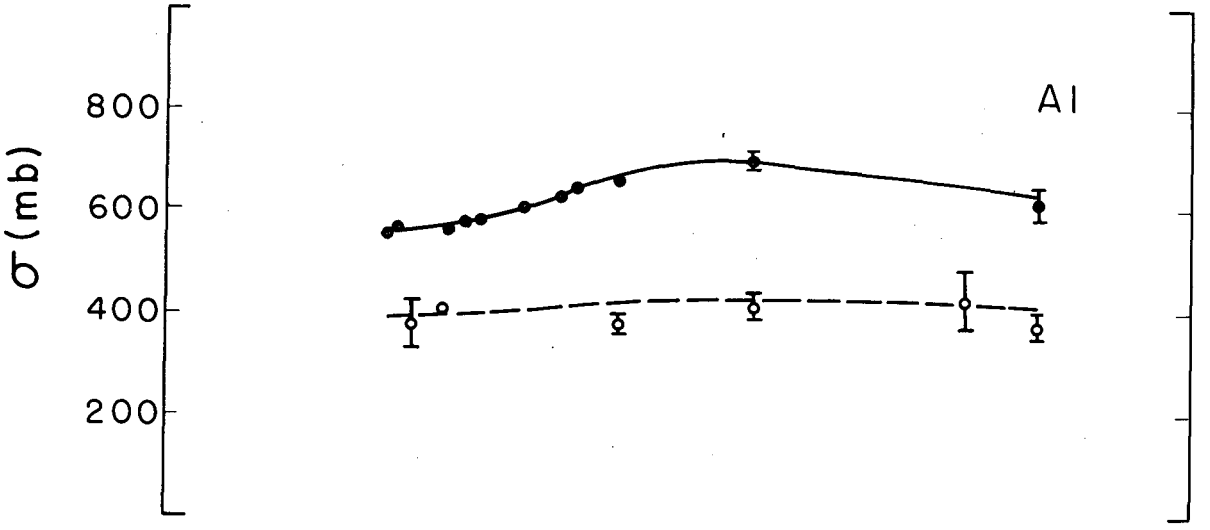

MU-18803

Fig. 21. Neutron total and reaction cross sections for aluminum. The solid curves are the theoretical total cross sections and the dashed curves are the theoretical reaction cross sections. The circles are the experimental measurements.

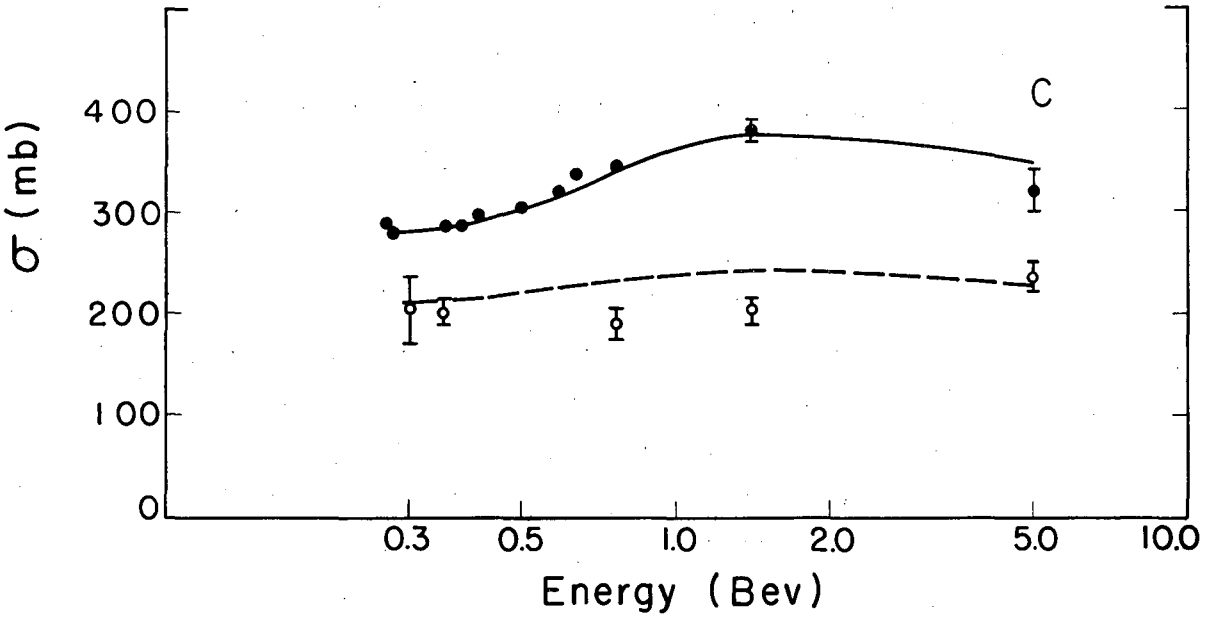

MU-18804

Fig. 22. Neutron total and reaction cross sections for carbon. The solid curves are the theoretical total cross sections and the dashed curves are the theoretical reaction cross sections. The circles are the experimental measurements.

p-p elastic cross section data of Cork and Wenzel[3] also exhibits the same drop, although not so dramatically as our data. The n-p reaction cross section (nonelastic) is very difficult to measure, and has not been measured above 300 Mev. The data on n-p cross sections as a function of energy are illustrated in Fig. 23.

However, the prediction by Williams[2] based on an optical-model theory that the nucleon-nucleon total cross section increases monotonically from 42 millibarns at 1.4 Bev to 120 mb at 30 Bev is now dubious. Again, the cosmic-ray data Williams used to justify this analysis are of a tenuous nature.

The increase in the nucleon-nucleon total cross section from the low point at about 300 Mev starts at the threshold for pion production. Furthermore, the peak of the nucleon-nucleon total cross section at 1.4 Bev occurs at roughly the threshold for strange-particle production. At higher energies, however, no mechanism reducing the total cross section is apparent. This observation indicates that nucleons become more transparent in nucleon-nucleon collisions as the incident-particle energy is increased from 1.4 to 5.0 Bev.

B. Interpretation

1. Generalized Diffraction Theory

Glassgold and Greider developed a generalized diffraction theory to explain the behavior of the neutron cross sections from 300 Mev to 5.0 Bev in the elements measured.[4] This theory uses the gross-average properties of the phase shifts to magnify small changes in the reaction cross section into large changes in the total cross section. It also crudely explains the cross sections for heavier elements in terms of the measured nucleon-nucleon cross section.

The usual expressions for the cross sections in terms of partial-wave analysis, as given by Blatt and Weisskopf,[16] are

$$\sigma_r = \pi \lambda\!\!\!^{-2} \sum_{\ell=0}^{\infty} (2\ell + 1) \left[1 - |\eta_\ell|^2 \right] , \qquad (14)$$

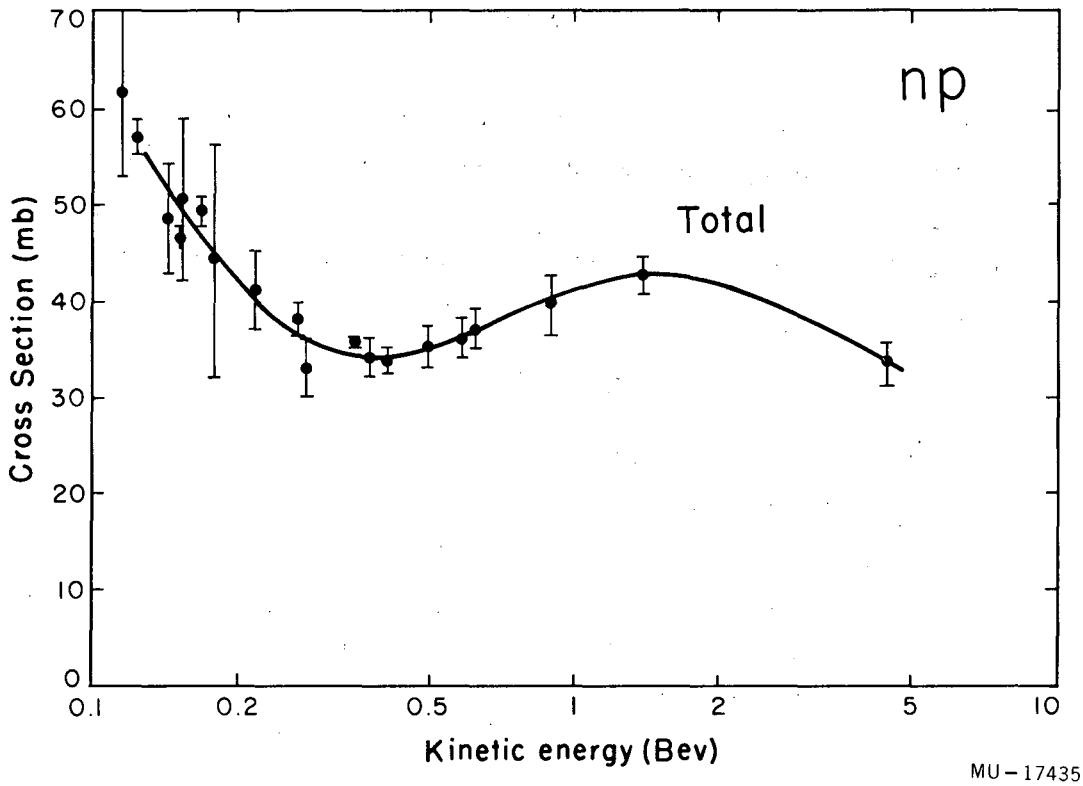

Fig. 23. Neutron total and reaction cross sections for hydrogen. The solid curves are the theoretical total cross sections and the dashed curves are the theoretical reaction cross sections. The circles are the experimental measurements.

$$\sigma_t = 2\pi\lambda\!\!\!^{-2} \sum_{\ell=0}^{\infty} (2\ell + 1) \quad [\, 1 - \mathrm{Re}\,(\eta_\ell)\,] \;, \tag{15}$$

$$f\,(\theta) = \frac{1}{2k} \sum_{\ell=0}^{\infty} (2\ell + 1)\,(1 - \eta_\ell)\, P_\ell\,(\cos\theta)\;, \tag{16}$$

where σ_r is the reaction cross section, σ_t is the total cross section, $\lambda\!\!\!^{-}$ is the wave length of the incoming particle, k is the wave number of the incoming particle, η_ℓ is the complex coefficient of the outgoing wave with angular momentum ℓ, and the sum is over the ℓ partial waves. We shall define

$$\eta_\ell = |\,\eta_\ell\,|\, e^{2i\sigma_\ell} \;, \tag{17}$$

where σ_ℓ is the usual phase shift for the ℓth partial wave. These cross sections are strictly valid only for spinless neutral particles.

These expressions readily give the cross sections for a black sphere. The effect of a black sphere that is completely opaque ($\eta_\ell = 0$) for interactions of angular momentum $\leqslant L$ and completely transparent ($\eta_\ell = 1$) for interactions of angular momentum $> L$ is illustrated in Fig. 24. Equations (14) to (16) then give directly, for the cross sections and the scattering amplitude,

$$\sigma_r = \pi\lambda\!\!\!^{-2} L^2 \;, \tag{18}$$

$$\sigma_t = 2\,\pi\lambda\!\!\!^{-2} L^2 \;, \tag{19}$$

$$f\,(\theta) = \frac{i}{2}\, L^2 \quad \frac{J_1\,(2L\sin\frac{\theta}{2})}{2\,L\sin\frac{\theta}{2}} \;. \tag{20}$$

If a radius of the nucleus is defined as the maximum radius at which an interaction can take place, then

$$L = pR = \frac{R}{\lambda\!\!\!^{-}} \qquad \text{and} \tag{21}$$

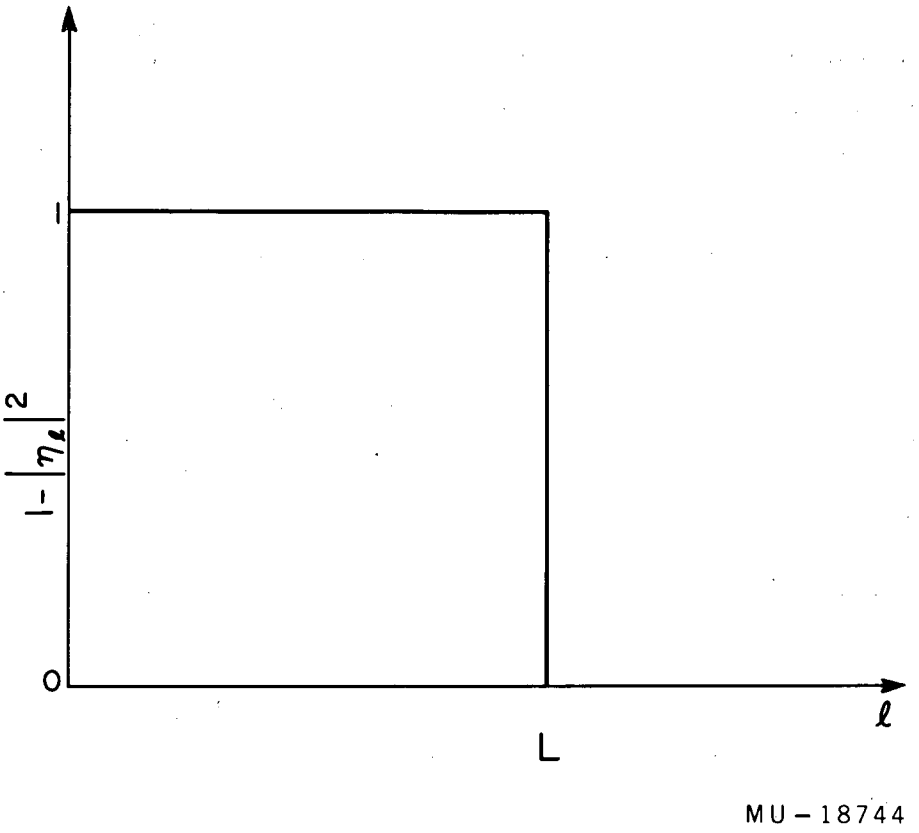

Fig. 24. Black-sphere model.

$$\sigma_r = \pi R^2 , \tag{22}$$

$$\sigma_t = 2\pi R^2 . \tag{23}$$

This simple model of the nucleus gives the ratio of σ_t/σ_r as 2, independent of energy. This is obviously not the case, as an inspection of Table IV reveals.

Table IV

Ratios of total to reaction cross sections

	Pb	Cu	Al	C
$\frac{\sigma_t}{\sigma_r}$	1.51 ± .10	1.98 ± .10	1.61 ± .14	1.36 ± .13

The new model by Glassgold and Greider describes high-energy scattering collisions in terms of four physically significant parameters. If constant phase is assumed,[19] these parameters are: L, the number of partial waves strongly absorbed; β, the opacity for small ℓ; 2Δ, the range over which the opacity function decreases from β to 0; and α, the phase of the outgoing wave. The relationship of these parameters is illustrated in Fig. 25. This model generalizes the simple diffraction theory by writing $\eta_\ell = |\eta_\ell| e^{i\alpha_\ell}$ (24) and by assuming (a) that the interaction region can be represented as a smooth function, i.e., that the opacity function, $1 - |\eta|^2$, decreases monotonically with ℓ from an essentially constant value β for small ℓ to zero for large ℓ, (b) that this transition occurs mainly within an interval of width 2Δ centered about a large value of the angular momentum L, and (c) that the phase function α is continuous and vanishes for sufficiently large ℓ.

The analytic expression of assumptions (a) and (b) is illustrated in Fig. 25. Using this analytic expression, one can find

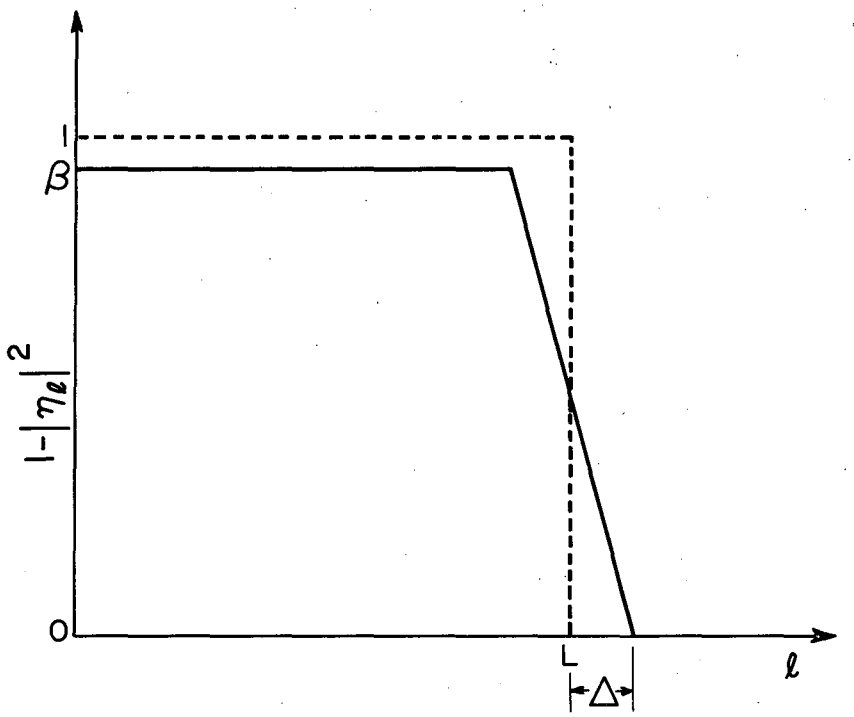

MU-18745

Fig. 25. Diffraction model of Glassgold and Greider. The dashed line gives the black-sphere model.

closed forms for the cross sections and scattering amplitude. Several functional forms for the fall-off shape were tried by Glassgold and Grieder, but the results were found to be independent of the details of this region. The assumption was also made that an integral over ℓ from 0 to $L+\Delta$ could replace the sum over ℓ. Since the values of L required are typically greater than 200, this substitution is valid to considerable accuracy at these high energies. With these assumptions, the cross sections and scattering amplitude, as expressed in Eqs. (14), (15), and (16), can now be evaluated directly. It is convenient to expand the solutions in powers of the small quantities σ and ϵ defined as

$$\sigma = (1 - \cos \alpha) \text{ and } \epsilon = \sqrt{1 - \beta} \quad . \tag{25}$$

Assuming a straight-line fall-off of $1 - |\eta_\ell|^2$ from β to zero between $L - \Delta$ and $L + \Delta$, the following forms are derived:

$$\frac{\sigma_r}{\pi \lambda\!\!\!^{-2}} = [L^2 + L + \frac{\Delta^2}{3}] \quad (1 - \epsilon^2) \tag{26}$$

$$\frac{\sigma_t}{2\pi \lambda\!\!\!^{-2}} = [L^2 - \frac{2}{3}\Delta L + \frac{7}{15}\Delta^2 + L - \frac{\Delta}{3}] \tag{27}$$

$$+ \epsilon[\ldots] + \epsilon^2[\ldots] + \sigma[\frac{8}{3}\Delta L + \frac{8}{15}\Delta^2 + \ldots]$$

$$+ \sigma\epsilon[\ldots\ldots] + \sigma\epsilon^2[\ldots\ldots],$$

$$f(\theta) = \frac{i}{K}(1 - \epsilon)\left[(L^2 - \frac{\Delta L}{4})\frac{J_1(a)}{a} + (L^2 + \Delta^2 - 2\Delta L - 2\Delta + 2L)\frac{J_1(a-b)}{(a-b)}\right.$$

$$+ \frac{\Delta L - L + \Delta}{2} \cos(b) \; J_0(a)$$

$$\left. + L^2 \sin^2\frac{\theta}{2}\left(\frac{J_0(a)}{6} - \frac{J_1(a-b)}{a-b}\right)\right]$$

where $a = 2(L+1)\sin\frac{\theta}{2}$ and $b = 2\Delta\sin\frac{\theta}{2}$.

2. Application of Theory to Experiments

The expressions obtained in Section 1 above can now be used to fit the experimental neutron-scattering data from 300 Mev to 5 Bev. Two reasonable assumptions are made: $L \propto k A^{1/3}$, where A is the atomic weight, and $\Delta \propto k$. The large variation in σ_t with energy while σ_a remains relatively constant requires that the phase α be small, as can be seen by comparison of Eqs. (14) and (15). In fact, the best fit to the data is for $\alpha = 0$.

For small real η, σ_t varies linearly with η and is therefore more sensitive to changes in η than σ_r, which varies quadratically in η. The theoretical fit to the experimental is given by the curves in Figs. 19, 20, 21, 22, and 23. The fit is seen to be quite good, particularly when the uncertainties in the neutron-cross-section measurements are considered. The values of L, Δ, and β used in the analysis are given in Table V.

Table V

Diffraction-model parameters

	Pb	Cu	Al	C
β (5 Bev)	0.94	0.94	0.93	0.89

$\Delta = 0.61\ k \times 10^{-13}$

$L = 1.26\ A^{1/3}\ k$

Consideration of the ratio

$$\frac{\sigma_t\ (\ell)}{\sigma_r\ (\ell)} = \frac{2\ (1 - n_e)}{1 - n_e^{\ 2}} = \frac{2}{1 + n_\ell} \qquad (29)$$

shows directly that this ratio of the total to the reaction cross section can be less than 2, as required by the data. Also, this ratio decreases as η_ℓ increases, that is, as the opacity function $(1 - |\eta|^2)$ decreases. The experimental values of this ratio are given in Table IV.

We can qualitatively understand β from a consideration of the nucleon-nucleon cross section. The dependence of β on k and A can be interpreted in terms of a classical picture of exponential absorption with distance, the absorption coefficient being related to the observed nucleon-nucleon total cross sections. Crudely β is given by

$$\beta = 1 - e^{-2R\rho\overline{\sigma}_t} , \tag{30}$$

where 2R is the maximum distance across the nucleus, ρ is the density of nucleons in the nucleus, and $\overline{\sigma_t}$ is the average nucleon-nucleon cross section. Computation of β using our measured value of 33.6 millibarns gives approximate agreement with the values of β given in Table V.

C. Optical Model

1. Theory

This experiment can also be analyzed in a more conventional manner by using the optical model of Fernbach, Serber, and Taylor.[17] This was the method of analysis used by Coor et al.[1] for their 1.4-Bev neutron-cross-section experiment. The uniform-density model is used here for simplicity although it is no more than a first approximation. This model describes the nucleus in terms of the nuclear radius R, the absorption constant K, and k_1, the increment in the wave number inside the nucleus. This experiment measured σ_t, the neutron total cross section; σ_r, the neutron reaction cross sections; and the mean energy of the incoming neutrons, which gives the neutron wave number k.

Fernbach, Serber, and Taylor give the following formulas for a sphere of radius R:

$$\sigma_r = 2\pi \int_0^R (1 - u^2)\, r dr = \pi R^2 \left\{ 1 \quad \frac{(1 - 2KR)e^{-2KR}}{2K^2R^2} \right\}, \quad (31)$$

$$\sigma_t = \sigma_r + \sigma_d = \sigma_r + 2\pi \int_0^R \left| (1 - u) \right|^2 r dr \,, \quad (32)$$

where u is the transmitted wave amplitude at impact parameter r,

$$u = \exp \left\{ - (k + ik_1)\, (R^2 - r^2)^{1/2} \right\} . \quad (33)$$

The absorption constant K can be expressed in terms of the average nucleon-nucleon cross section, $\bar{\sigma}$:

$$K = \frac{A\bar{\sigma}}{(4/3)\,\pi R^3} \,, \qquad \text{or} \qquad KR = \frac{A\,\bar{\sigma}}{(4/3)\,\pi R^2} \,. \quad (34)$$

Likewise, k_1 can be given in terms of the nucleon-nucleon forward scattering amplitude $f(0)$,

$$k_1 = (2\pi\rho/k)\ \mathrm{Re}\, f(0), \quad (35)$$

where ρ is the nuclear density. The elastic differential scattering cross section is given by

$$\frac{d\sigma_d}{d\Omega} = k^2 \left| \int_0^R (1-u)\, J_0\, (kr \sin\theta)\, r\, dr \right|^2 . \quad (36)$$

As discussed in Section III. A. 2, this is very similar in angular distribution to the diffraction scattering from a cylinder, thus

$$\frac{d\sigma_d}{d\Omega} \sim \left[\frac{J_1\, (kR \sin\theta)}{\sin\theta} \right]^2 . \quad (6)$$

As before, we define

$$F(\theta) = \frac{1}{\sigma_d} \int_0^{\theta} \frac{d\sigma_d}{d\Omega} \, d\Omega \, . \tag{9}$$

Now, $F(\theta)$ depends almost exclusively on the parameter kR and is insensitive to the values of KR and k_1/K. Furthermore, Coor et al. show that the values of $F(\theta)$ depend primarily on $\langle k \rangle$ (the mean value of k), and are independent of the spectrum of k values for fixed R. Then they give the relationship

$$\langle k \rangle \; R\,\theta_{1/2} = 1.7 \, , \tag{37}$$

where $F(\theta_{1/2}) = 0.5$ defines $\theta_{1/2}$.

2. Optical Model Parameters

The optical-model parameters can now be evaluated by using the equations of Section 1 and the data of this experiment. The nuclear radius R is obtained by combining Eqs. (31) and (34) and using our measured n-p total-cross-section value of 34 millibarns for $\bar{\sigma}$. The combination gives

$$\sigma_r = \pi R^2 \left\{ 1 - \frac{\left(1 - \frac{3A\bar{\sigma}}{2\pi R^2}\right) e^{-\frac{3A\bar{\sigma}}{2\pi R^2}}}{\frac{9}{8} \frac{A^2\bar{\sigma}^2}{\pi^2 R^4}} \right\} . \tag{38}$$

Graphs of σ_r versus R are given in Figs. 26 through 29 for the various elements measured. Equation (34) then gives KR for each element.

To obtain k_1 we combine Eqs. (31), (32), and (33) to give the ratio

$$\frac{\sigma_t}{\sigma_r} = 1 + \frac{2\pi}{\sigma_r} \int_0^R \left| 1 - e^{-(K + ik_1)(R^2 - r^2)^{1/2}} \right|^2 r\,dr . \tag{39}$$

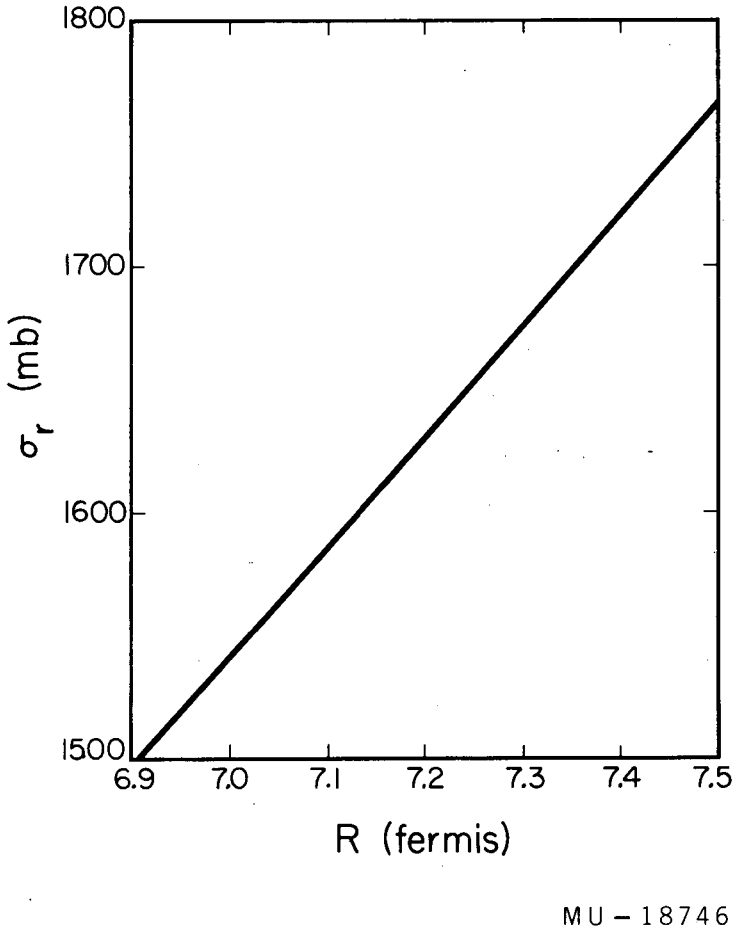

Fig. 26. Uniform-density model nuclear radius vs reaction cross section for lead.

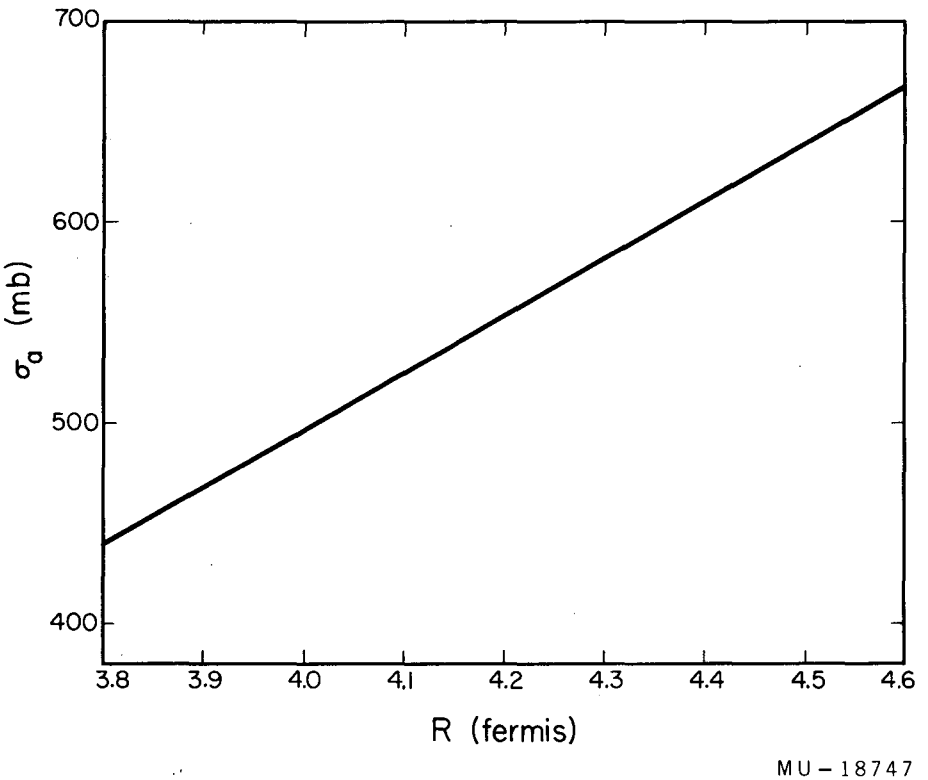

Fig. 27. Uniform-density model nuclear radius vs reaction cross section for copper.

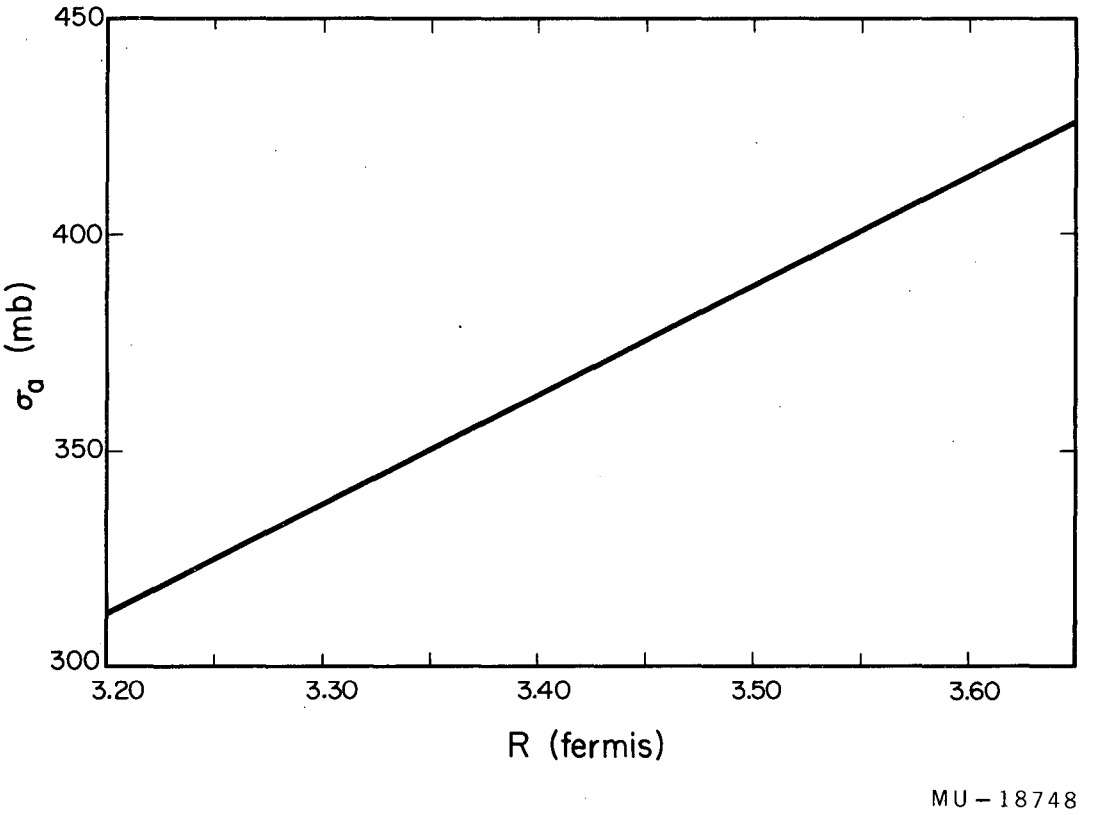

Fig. 28. Uniform-density model nuclear radius vs reaction cross section for aluminum.

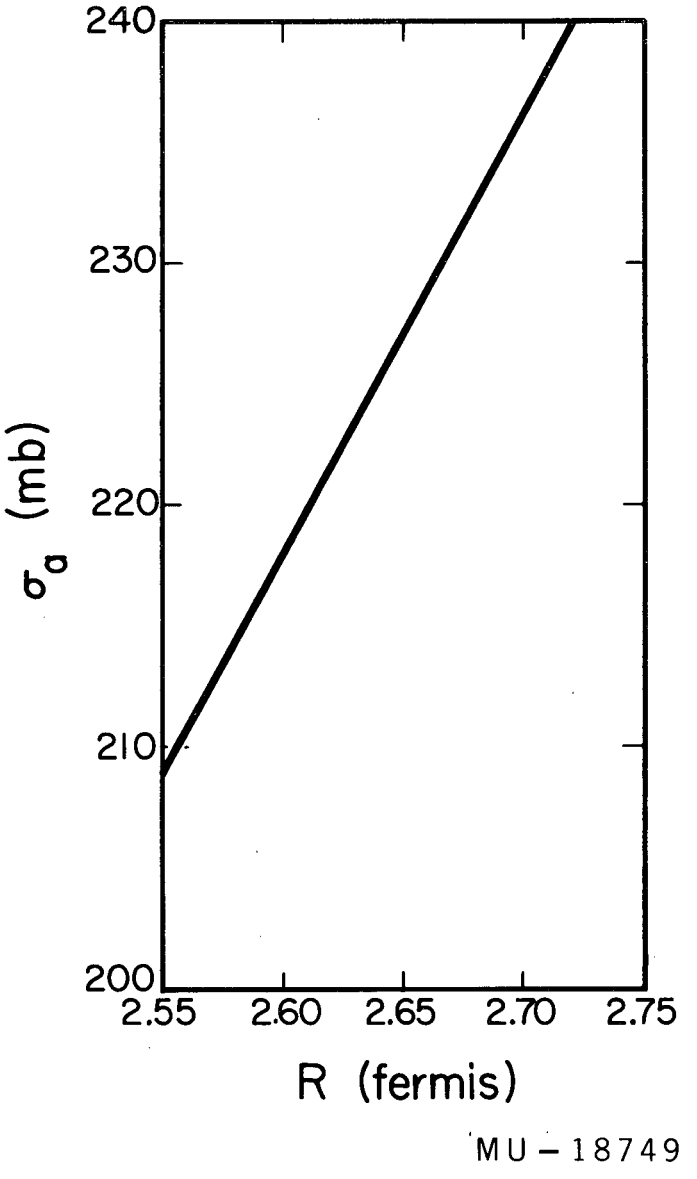

Fig. 29. Uniform-density model nuclear radius vs reaction cross section for carbon.

This is integrated to give

$$\frac{\sigma_t}{\sigma_r} = 1 + \frac{\pi R^2}{\sigma_r} \left\{ 1 - \frac{e^{-2KR}}{2(KR)^2}(2KR+1) + \frac{1}{2(KR)^2} + \frac{4}{(KR)^2\left(1+\frac{k_1^2}{K^2}\right)^2} \right.$$

$$\left(e^{-KR} \left[\frac{k_1}{K} \left(KR \left\langle 1 + \frac{k_1^2}{K^2} \right\rangle + 2 \right) \sin \frac{k_1}{K} KR - \left(KR \left[1 + \frac{k_1^2}{K^2} \right] - \left[1 - \frac{k_1^2}{K^2} \right] \right) \right.\right.$$

$$\left. \left. \cos \frac{k_1}{K} KR \right] + \left(1 - \frac{k_1^2}{K^2} \right) \right\} \tag{40}$$

A value of $\frac{k_1}{K}$ is then chosen which gives agreement with $\frac{\sigma_t}{\sigma_r}$ for all the elements thus determining a mean value of k_1 in terms of K. An average value of K may be obtained by making a least-squares fit of the observed R plotted versus $A^{1/3}$, giving r_0 of

$$R = r_0 A^{1/3} \times 10^{-13} \text{ cm} . \tag{41}$$

Then, from Eq. (34),

$$K = \frac{\bar{\sigma}}{\frac{4}{3}\pi r_0^3 \times 10^{-39}} \text{ cm}^{-1} . \tag{42}$$

Although its significance at these energies is doubtful, average nuclear $\bar{V}$ potential is given by

$$k_1 = \frac{\bar{V}}{\hbar c \beta} . \tag{43}$$

3. Optical-Model Results

Application of Eq. (40) to our data for carbon, aluminum, copper, and lead gives the fits illustrated in Fig. 30. The best fit is given for $\frac{k_1}{K} = 0.4 \pm .2$, although even this value is somewhat arbitrary. The least-squares fit of the data to Eq. (41) gives a value for r_0 of $(1.17 \pm .06) \times 10^{-13}$ cm. Equation (42) is then solved for K, giving $K = (5.02 \pm .35) \times 10^{12}$ cm^{-1}. Finally a value of $k_1 = (0.2 \pm 0.1) \times 10^{13}$ is derived from the ratio $\frac{k_1}{K}$. Equation (43) then gives the average nuclear potential as 39.1 ± 19.5 Mev. These parameters have essentially the same values as those derived by Coor et al. Within the large experimental errors.

The data furnish some information on nuclear radii. The uniform-density optical model gives a value for r_0 of $(1.17 \pm .06) \times 10^{-13}$ cm. Glassgold and Greider's diffraction theory[4] gives values of L, the number of partial waves strongly absorbed. A nuclear radius R may be defined as $L - Rk - r_0 A^{1/3} k$. The analysis by Glassgold and Greider gives a value of r_0 of 1.26×10^{-13} cm. These values are comparable to the value of $r_0 = 1.28 \times 10^{-13}$ which Coor et al. derived from 1.4-Bev neutron scattering and the value of the electromagnetic size of the nucleus, $r_0 = 1.19 \times 10^{-13}$, for an equivalent square-well potential derived from electron-scattering experiments of Hofstadter.[18]

Finally, the mean energy of the incoming neutron beam is given by Eq. (37). This was the method used by Coor et al. to determine the mean energy of their neutron beam. For this experiment, this method gives a check on the mean energy derived from the calculated effective neutron spectrum. The data for lead are the most extensive as a function of subtended angle. The diffraction pattern for lead gives a mean neutron energy of 5.3 ± 2.3 Bev. This compares well to the mean neutron energy of $5 \pm .4$ Bev derived in Section II. C. 1.

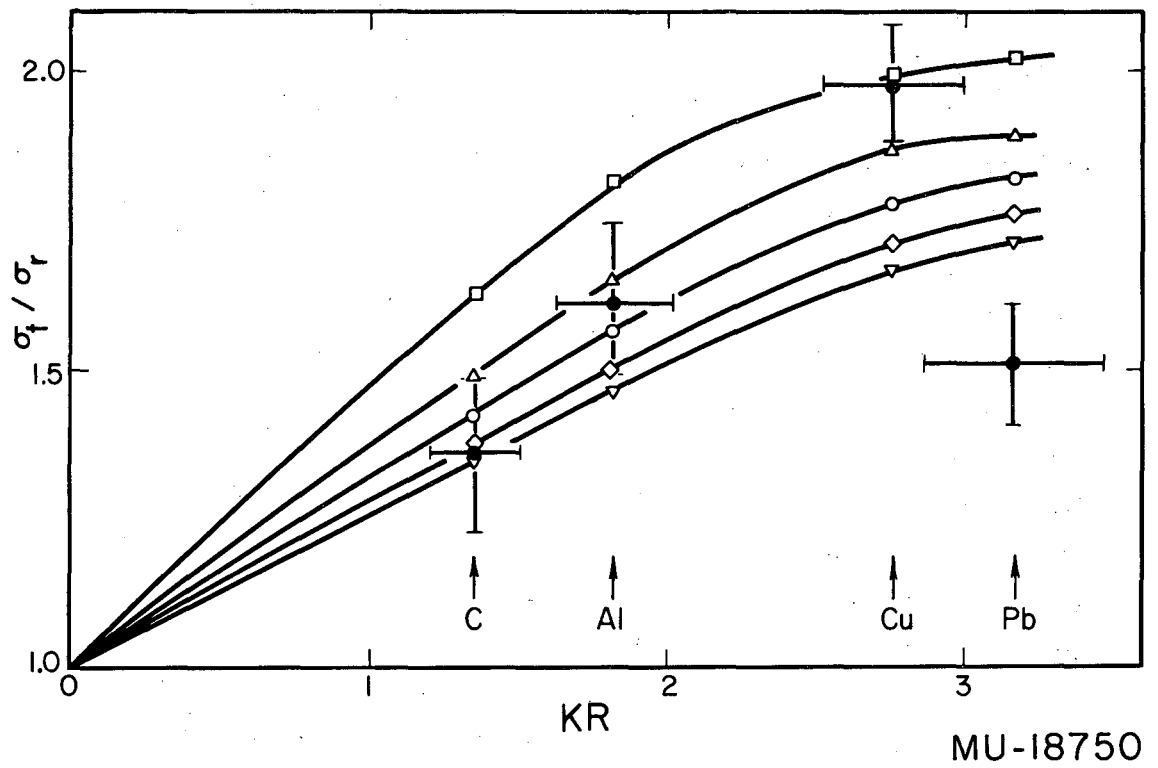

Fig. 30. Experimental point of σ_t/σ_r vs KR and the corresponding theoretical curves for various values of $k_1 / \bar{K}$, using the uniform density model; R, K, and k_1 are the optical-model parameters for a uniform sphere.

ACKNOWLEDGMENTS

I should like to express my appreciation to the many people whose help was necessary for the successful completion of this long experiment. I thank Professor A. Carl Helmholz and Professor Burton J. Moyer for their support and encouragement of this experiment. My collaborators, Dr. Victor Perez-Mendez, Dr. Wilmot N. Hess, and Dr. Roger W. Wallace were instrumental in the success of this experiment. I wish to thank Mr. Richard Kurz and Mr. Donald Hagge for accepting responsibility in the running and analysis of this experiment. I am grateful to the following for taking data on many long shifts at the Bevatron: Julius Solomon, Barry Barish, William P. Swanson, Duane C. Gates, Donald McPherson, Alden McLellan, Calvin Wood, Jackson R. Pickens, John N. Green, and James Beaseley. Mr. Michael Scadron and Mr. George Buonocore completed the statistical analysis of the data as well as taking data. I would like to thank Dr. Robert Kenney for his support and Mr. Duane Newhart for his help in the construction and operation of the hydrogen target.

Finally, I wish to thank Dr. Edward J. Lofgren and Dr. William A. Wenzel for their tolerance in my extended use of the Bevatron. Also I am most grateful to Mr. Walt Hartsough and the Bevatron crew for their courteous cooperation during the long run of this experiment.

This work was done under the auspices of the U.S. Atomic Energy Commission.

REFERENCES

1. Coor, Hill, Hornyak, Smith, and Snow, Phys. Rev. 98, 1369 (1955).
2. Robert W. Williams, Phys. Rev. 98, 1393 (1955).
3. Cork, Wenzel, and Causey, Phys. Rev. 107 859 (1957).
4. A. E. Glassgold and K. Greider, Phys. Rev. Lett. 2, 169 (1959).
5. D. Swift and Victor Perez-Mendez, Millimicrosecond Discriminator, UCRL-8569, Dec. 1958.
6. I. Frank and I. Tamm, Compt. rend. acad. sci. U.R.S.S. 14, 109 (1937).
7. J. Marshall, Ann. Rev. Nuclear Sci, 4, 141 (1954).
8. John Atkinson and Victor Perez-Mendez, Rev.Sci.Instr. (to be published).
9. Fred N. Holmquist, Pion Production in Neutron-Proton Collisions at Bevatron Energies, UCRL-8559, Dec. 1958.
10. Paul H. Barrett, Phys. Rev. 114, 1374 (1959).
11. Fredrick Wikner, Nuclear Cross Sections for 4.2-Bev Negative Pions, UCRL-3639, Jan. 1957.
12. L. Van Rossum and L. T. Kerth, Bull. Am. Phys. Soc., Series II, 1, 385 (1956). Frances M. Smith, Harry H. Heckman, and Walter H. Barkas, Composition of a Secondary-Particle Beam from the Bevatron, UCRL-3289, March 1956. Chupp, Goldhaber, Goldhaber, Johnson, and Webb, Nuovo cimento, N. 2, Suppl. 1, Vol. 4, Ser. X, 359 (1956). Production of K^0 mesons is assumed similar to $K^{\pm}$ production.
13. Cronin, Cool, and Abashian, Phys. Rev. 107, 1121 (1957).
14. Rossini and Deming, J. Wash. Acad. Sci., 29, 416 (1939).
15. Sinha and Das, Phys. Rev., 105, 1587 (1957).
16. Blatt and Weisskopf, "Theoretical Nuclear Physics," p. 317 ff. (1954).
17. Fernbach, Serber and Taylor, Phys. Rev., 75, 1352 (1949).
18. Robert W. Williams, Phys. Rev., 98, 1387 (1955), Robert Hofstadter, Rev. Mod. Phys., 28, 214 (1956); D. G. Ravenhall, Rev. Mod. Phys., 30, 430 (1958)

19. The case of nonconstant phase is discussed by Glassgold and Greider, Generalized Diffraction Theory for Very-High-Energy Scattering, Phys. Rev. (to be published). The assumption of nonconstant phase does not affect the cross section expressions.

This report was prepared as an account of Government sponsored work. Neither the United States, nor the Commission, nor any person acting on behalf of the Commission:

A. Makes any warranty or representation, expressed or implied, with respect to the accuracy, completeness, or usefulness of the information contained in this report, or that the use of any information, apparatus, method, or process disclosed in this report may not infringe privately owned rights; or

B. Assumes any liabilities with respect to the use of, or for damages resulting from the use of any information, apparatus, method, or process disclosed in this report.

As used in the above, "person acting on behalf of the Commission" includes any employee or contractor of the Commission, or employee of such contractor, to the extent that such employee or contractor of the Commission, or employee of such contractor prepares, disseminates, or provides access to, any information pursuant to his employment or contract with the Commission, or his employment with such contractor.